



# Dynamic response analysis of a motor–gear transmission system considering the rheological characteristics of magnetorheological fluid coupling

Hang Gong · Ruizhi Shu · Yang Xiong · Zhengqiu Xie · Jin Huang · Rulong Tan · Qin Yin · Zheng Zou

Received: 6 October 2022 / Accepted: 14 May 2023 / Published online: 21 June 2023  
© The Author(s), under exclusive licence to Springer Nature B.V. 2023

**Abstract** This study develops a method to suppress the mechanical vibrations of a motor–gear transmission system (MGTS) due to speed and external load variations. It also achieves soft starting of the drive motor using a magnetorheological fluid coupling (MRFC) with variable stiffness and damping instead of the traditional rigid coupling. Therefore, a mechanical–electromagnetic coupled dynamics model of an MGTS is established, which includes a drive motor, a gear transmission system, an MRFC, and a load. Based on the developed dynamics model, the effects of the MRFC on the dynamic response of the MGTS at different coil currents in the startup and stable operation stages of the drive motor are investigated. The results show that as the coil current increases, the coil current overshoot increases, and the overshoot

duration is 0.125 s. When the current is 2.0 A, the coil current overshoot reaches a maximum, and the overshoot rate is 8.84%. Concurrently, when the coil current increases from 0.5 to 2.0 A, the magnetic field intensity in the MRF working area increases from 0.38 to 0.74 T, the torque increases from 70 to 115 N·m, and the response time of the MRFC reduces from 0.125 to 0.002 s. Moreover, the relative vibration center offset rates (RVCORs) in the  $x$ ,  $y$ , and  $\theta$  directions of nodes 4, 8, 10, and 15 gradually decrease with increasing coil current. However, these RVCORs reach maximum when the coil current is 2.0 A, with those in the  $x$  direction being 0.586%, 0.447%, 0.446%, and  $-0.263\%$ , respectively, and in the  $y$  direction being 0.586%, 0.451%, 0.497%, and  $-0.264\%$ , respectively. The RVCORs of the helical gear meshing node of the MGTS in the  $\theta$  direction are 0.0722%. Furthermore, the maximum vibration amplitude reduction rates (MVARRs) in the  $x$ ,  $y$ , and  $\theta$  directions of nodes 4, 8, 10, and 15 gradually increase with increasing coil current. The MVARRs of each node reach the maximum when the coil current is 2.0 A; the MVARRs of nodes 4, 8, 10, and 15 in the  $x$  direction are 40.98%, 83.4%, 83.49%, and 2.17%, respectively, and those in the  $y$  direction are 64.4%, 83.4%, 83.46%, and 2.16%, respectively. The MVARRs of the helical gear meshing node in the  $\theta$  direction have an MVARRs of 29.1%. Moreover, the vibration amplitudes of the gear meshing node decay the fastest in the  $\theta$  direction, and the decay time

---

H. Gong · R. Shu (✉) · Z. Xie · J. Huang · R. Tan · Q. Yin · Z. Zou  
Department of Mechanical Engineering, Chongqing University of Technology, Chongqing 400054, People's Republic of China  
e-mail: ruizhishu@cqut.edu.cn

R. Shu  
The State Key Laboratory Mechanical Transmissions, Chongqing University, Chongqing 400054, People's Republic of China

Y. Xiong  
Department of Mechanics and Engineering Science, Shanghai University, Shanghai 200444, People's Republic of China

reduces from 2.8 to 0.3 s when the coil current increases from 0.5 to 2.0 A.

**Keywords** Motor–gear transmission system · Dynamic response · MRFC · Vibration amplitude reduction rate

### Abbreviations

$V$	Coil voltage	$C_c$	Critical damping coefficient of MRFC
$I$	Coil current	$\omega_n$	Angular frequency
$L$	Coil inductance	$\xi_M$	Damping ratio
$R$	Coil resistance	$K_M$	Stiffness matrix of MRFC
$V_0$	Constant voltage	$M_M$	Mass matrix of MRFC
$t$	Time	$C_M$	Damping matrix of MRFC
$\tau$	Shear stress of MRF	$X_M$	Displacement matrix of MRFC
$\eta$	Zero-field viscosity of MRF	$K_s$	Stiffness matrix of shafting element
$\tau_{(H)}$	Dynamic yield stress of MRF	$M_s$	Mass matrix of shafting element
$\dot{\gamma}$	Shear strain rate of MRF	$C_s$	Damping matrix of shafting element
$B$	Magnetic flux density	$X_s$	Displacement matrix of shafting element
$H$	Magnetic field intensity	$e$	Transmission error
$\mu_0$	Vacuum magnetic permeability of MRF	$x_{j+1}, y_{j+1}, z_{j+1}$	Translation displacement of nodes $j + 1$
$\mu_r$	Relative magnetic permeability of MRF	$\theta_{x_j}, \theta_{y_j}, \theta_{z_j}$	Rotational angular displacement of nodes $j$
$R_1$	Radius of driven cylinder	$\theta_{x_{j+1}}, \theta_{y_{j+1}}, \theta_{z_{j+1}}$	Rotational angular displacement of nodes $j + 1$
$R_2$	Radius of driving cylinder	$m_j, I_{ij}$	Mass and moment of inertia to nodes $j$
$\Delta\omega$	Speed difference between input and output	$m_{j+1}, I_{ij+1}$	Mass and moment of inertia to nodes $j + 1$
$l$	Working gap length of MRF	$E$	Elastic modulus of shaft material
$l_e$	Effective working gap length of MRF	$P$	Moment of inertia of section
$E_M$	Relative shear modulus of MRF	$\varsigma$	Shear influence factor
$E'$	Storage modulus of MRF	$a$	Length of beam element
$E''$	Loss modulus of MRF	$G_m$	Shear elastic modulus of shaft material
$\varrho$	Volume fraction of MRF	$A$	Cross-sectional area of beam element
$B_s$	Magnetization intensity of MRF	$j$	Polar moment of inertia
$\lambda$	Loss factor	$n$	Section influence coefficient
$k_M$	Torsional stiffness coefficient of MRF	$p$	Mass scaling coefficients
$c_M$	Torsional damping coefficient of MRF	$q$	Stiffness scaling coefficients
$J_M$	Rotational inertia of MRFC	$\zeta_1, \zeta_2$	Damping coefficient
		$\omega_2$	Intrinsic frequency
		$\alpha$	Pressure angle

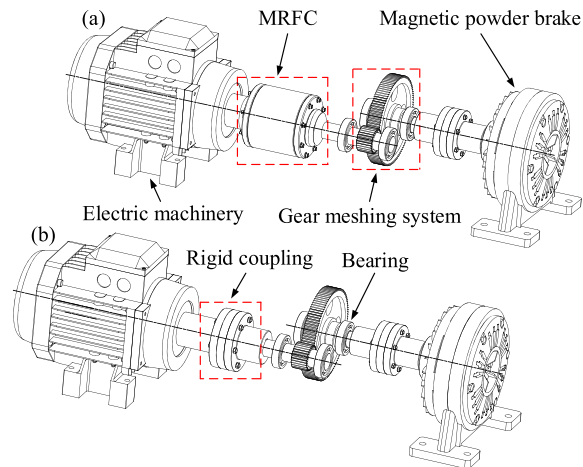
$\gamma$	Angle (between the gear meshing line and the $y$ -axis)	$k_{zz}$ $k_{\theta_x\theta_x}, k_{\theta_y\theta_y}$ $G_S$	Axial stiffness Torsional stiffness Gyroscopic matrix of shaft element
$\beta_b$	Helical angle		
$r_1, r_2$	Base radiuses of driving gear and driven gear	$K_C$	Stiffness matrix of connecting element
$K_G$	Stiffness matrix of gear meshing element	$C_C$	Damping matrix of connecting element
$C_G$	Damping matrix of gear meshing element	$M_C$	Mass matrix of connecting element
$X_G$	Displacement matrix of gear meshing element	$X_C$	Displacement matrix of connecting element
$M_G$	Mass matrix of gear meshing element	$T_{in}$	Input torque of drive motor
$x_{xi}, x_{yi}, x_{zi}$	Translational displacement of the driving gear	$T_{load}$ $M$ $K$	Load torque Mass matrix of MGTS Stiffness matrix of MGTS
$\theta_{z1}, \theta_{z2}$	Rotational angular displacement	$C$ $X(t)$	Damping matrix of MGTS Whole displacement vector of MGTS
$x_2, y_2, z_2$	Translational displacement of the driven gear	$F(t)$	System external load column vector
$\delta$	Relative total deformation	$T$	MRF transmission torque of MRFC
$x_j, y_j, z_j$	Translation displacement of nodes $j$	$T_L$	Load torque
$V_G$	Meshing matrix of helical gear pair	$X_x$ $X_y$	Amplitude of $x$ -direction Amplitude of $y$ -direction
$m_1, m_2$	Mass of the driving and driven gear	$X_\theta$ $x_o$	Amplitude of $\theta$ -direction Vibration center of $x$ -direction
$I_{x1}, I_{y1}, I_{z1}, I_{x2}, I_{y2}, I_{z2}$	Rotational inertia of the driving and driven gear	$y_o$	Vibration center of $y$ -direction
$f_s$	Normal force of the helical gear pair	$\theta_o$	Vibration center of $\theta$ -direction
$k_m$	Helical gear pair meshing stiffness	$\varepsilon$	Relative vibration center offset rate
$c_m$	Helical gear pair meshing damping	$x_M$	Maximum vibration amplitude of $x$ -direction
$F_G$	External excitation force column vector	$y_M$	Maximum vibration amplitude of $y$ -direction
$K_B$	Stiffness matrix of bearing element	$\theta_M$	Maximum vibration amplitude of $\theta$ -direction
$C_B$	Damping matrix of bearing element	$\phi$	Amplitude reduction rate
$M_B$	Mass matrix of bearing element	$\rho$ $G_G$	Density of shaft material Gyroscopic matrix of helical gear pair
$X_B$	Displacement matrix of bearing element	$\Omega$	Spin speed
$k_{xx}, k_{yy}$	Radial stiffness	$r_s$	Radius of gyration

$G$	Whole gyroscopic matrix of MGTS
$\Omega_1, \Omega_2$	Rotation angular speed

## 1 Introduction

A magnetorheological fluid (MRF) is a new type of solid–liquid two-phase intelligent material, and it can rapidly (20–300 ms) undergo a reversible transformation from a free-flowing to solid-like state, whose working properties are constrained and controlled by an applied magnetic field [1, 2]. The rheological properties of an MRF, when described quantitatively in terms of changes in viscosity, are explained as follows. In the presence of a magnetic field, the apparent viscosity (0.1–1.1 Pa·s) of an MRF is typically several orders of magnitude higher than in its absence, causing its stiffness and damping coefficients to also increase tens of thousands of times. Therefore, the mechanical properties of an MRF such as elastic modulus are appropriately controlled by a magnetic field [3–5]. Owing to the excellent mechanical behavior of MRF, their application to vibration reduction has been investigated. Olivie et al. [6] proposed a new hybrid annular radial magnetorheological damper to improve the smoothness of new energy vehicles. Masaharu et al. [7] proposed a two-degree of freedom dynamics model for an MRF shock absorber and experimentally verified the feasibility and accuracy of the model. Ashok et al. [8] conducted experiments and observed that at high amplitude and frequency, the damping force and stiffness of an MRF increased significantly with an appropriate increase in the current. Feng et al. [9] designed a magnetorheological damper based on the extended constant deceleration control method, and it achieved a large controllable speed range and a large controllable damping force. The above studies quantitatively analyzed the relationship between the current and the damping force, and the results showed that an MRF suppresses mechanical system vibrations by controlling the damping force of the MRF damping device. However, they ignored the coupled effect of MRF damping devices with a motor–gear transmission system (MGTS) on the dynamic response and vibration characteristics of the latter.

An MGTS is a typical nonlinear electromechanical coupled transmission system and widely used in electric vehicles, aerospace, ocean engineering, and other mechanical equipment [10, 11]. With the development of electromechanical coupled systems with high integration and precision, the excessive mechanical vibrations caused by the changes in speed and external load are becoming increasingly prominent. These are one of the main causes reducing the service life of mechanical components and endangering the stability of system operations [12, 13]. Until now, many studies have been conducted on the nonlinear dynamic response characteristics and vibration and noise suppression of MGTS. Regarding the former, Jiang et al. [14] established a nonlinear gear dynamic model of an MGTS considering multifrequency excitations and analyzed the influence of single- and multifrequency excitations on its dynamic response. Zhu et al. [15] built a lumped parameter dynamic model of an MGTS and investigated the effects of the gear meshing stiffness, transmission error, and gear backlash on its nonlinear dynamic characteristics. Li et al. [16] proposed a multi-degree of freedom gear nonlinear model and studied the influence of the bearing support stiffness, gear backlash, and bearing clearance on the dynamic response characteristics of a gear system. Wang et al. [17] used the lumped mass method to establish a nonlinear dynamics model of the spur gear system and analyzed the influence of system parameters on its nonlinear dynamics characteristics. Li et al. [18] proposed a nonlinear dynamics model of planetary gear transmission considering nonlinear error excitations and segmental backlash nonlinearity and analyzed its nonlinear dynamics characteristics. Regarding vibration and noise suppression, Geng et al. [19] proposed a new rigid–flexible gear using a metal rubber and applied it to a transmission system to reduce gear vibrations and improve its stability. Lee et al. [20] used a new Fe–Mn damping alloy to manufacture mechanical components to reduce the vibration of a mechanical system. Ma et al. [21] developed a finite element model of a gear system and analyzed the effect of different gear tooth tip modifications on the time-varying mesh stiffness, dynamic transfer errors, and system vibration response. Bonori et al. [22] proposed a distinct genetic algorithm for optimizing the structural parameters of gear pairs to reduce the vibrations and noise of a gear transmission system. Xu et al. [23] developed a lightweight, low-amplitude gear plate design method to reduce the

**Fig. 1** Three-dimensional model of MGTS

(a) Transmission system with MRFC, (b) Transmission system with rigid coupling

vibrations of a gear transmission system. Xiao et al. [24] established an energy dissipation model of a gear transmission system under centrifugal load considering the characteristics of powder materials. They analyzed the influence of the size and damping of the powder materials on its vibration characteristics under extremely harsh operating conditions, and the results showed that the powder materials had a certain but insignificant vibration reduction effect. Ramadani et al. [25] reduced the vibrations of a gear transmission system by adding a polymer material to the gear bodies. Wang et al. [26] established a nonlinear dynamics model of a gear damping ring system and analyzed the influence of the embedded damping ring on the vibration reduction in a gear transmission system. However, most of the above studies treated an MGTS as a combination of noncorrelated mechanical and electrical parts. Moreover, they paid significant attention to the effects of system parameters on its dynamic response characteristics and only established a nonlinear dynamic model of a gear system without considering the drive motor. In addition, most studies preferred to use damping materials and performed gear modification and parameter optimization to reduce the vibrations and noise of an MGTS. Although the above methods have certain vibration suppression and noise reduction effects, they are nonideal because stiffness and damping cannot be changed by varying the operation conditions. Therefore, in this study, to obtain a more ideal vibration reduction effect, the traditional rigid coupling is replaced by magnetorheological fluid coupling (MRFC) with variable stiffness and damping. The

MRFC connects the drive motor and gear transmission system in an MGTS, as shown in Fig. 1.

The innovations of this study are the first use of an MRF as a vibration-reduction material in an MGTS and establishment of a new flexible MGTS including MRFC. By controlling the coil current of the MRFC, its magnetic field density and magnetic flux intensity are controlled to adaptively vary the stiffness and damping coefficients of the MRF. This suppresses the vibrations caused by abrupt load changes and achieves the motor soft start goal. Moreover, to more realistically reflect the vibration characteristics and dynamic response of the MGTS, a mechanical–electromagnetic coupled dynamics model is established, which includes a drive motor, a gear transmission system, MRFC, and a load. Based on the model, the research focuses on the influence of the MRFC coil current variation on the dynamic response characteristics and vibration reduction in the system in the drive motor startup and stable operation stages. The results show that the vibration amplitude of the MGTS decreases significantly with the increase in the coil current. The remainder of this paper is organized as follows. In Sect. 2 and 3, the established theoretical model of MRFC and the developed mechanical–electromagnetic coupled dynamics model are presented, respectively. In Sect. 4, the effects of MRFC and traditional rigid coupling on the dynamic response characteristics of each mechanical part of an MGTS are compared and the analysis results are discussed. In Sect. 5, the conclusions of this study are summarized.

## 2 Theoretical model of MRFC

### 2.1 Working principle of MRFC

A schematic of the structure of a cylindrical MRFC is shown in Fig. 2. The device mainly consists of an MRF, an input shaft, a coil, an output shaft, a brush slip ring, and other components. The MRF is located between the driving and driven cylinders, and the driving cylinder is connected to the motor output load terminal, and the output shaft is connected to the driving gear. MRFCs operate mainly on the shear yield stress of the MRF to transmit a torque. Varying the coil current controls the amount of torque transmitted, enabling the magnetostatic shear modulus, torsional stiffness, and damping coefficient of the MRF to be controlled by the current. Thus, the connection characteristics of the transmission system are changed, and the transmission system vibration is reduced.

### 2.2 Response characteristics of coil current

The current response characteristics are the excitation coil inside the MRFC detecting a change in the current from the generation of magnetic field intensity to the magnetic field for the MRF to produce stable magnetorheological effect. The simplified circuit structure of the MRFC is shown in Fig. 3.

Neglecting the effect of eddy currents inside the MRFC, the voltage drop across the coil and the applied current satisfies the following equation:

$$V(t) = L \frac{dI(t)}{dt} + RI(t) \tag{1}$$

where  $L$  is the coil inductance,  $t$  is the current loading time, supplying constant voltage source to the coil, Eq. (1) can be expressed as:

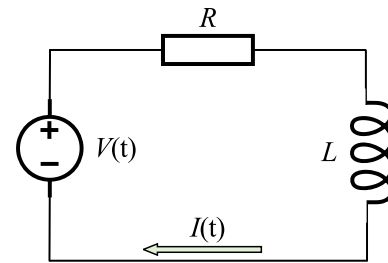


Fig. 3 Simplified circuit structure

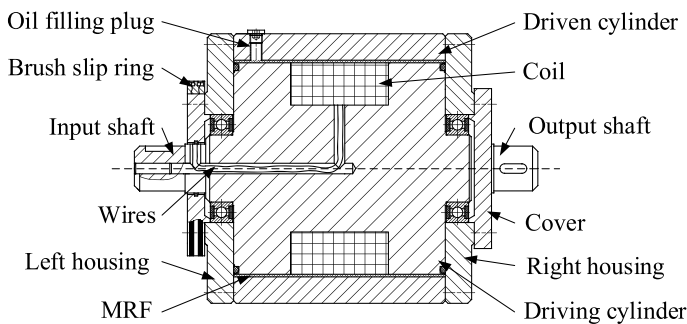
$$I(t) = L \frac{V_0}{R} (1 - e^{-\frac{Rt}{L}}) \tag{2}$$

where  $V_0$  is supply voltage, and combined with Eq. (2), the current response curve versus time can be derived as shown in Fig. 4.

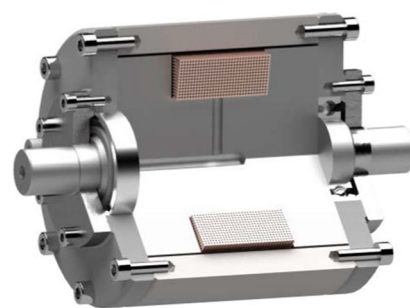
Current overshoot can occur during current loading, in the overshoot phase, in which the current becomes higher than the initial current value and stabilizes. In Fig. 4, the overshoots of the different currents start from 0.165 s. Each current returns to a steady state after 0.29 s, after an overshoot time of 0.125 s, and as the current increases, and the maximum overshoot rate of the current increases with the preset value. The maximum overshoot rates at the different currents are 2.2%, 4.75%, 6.86%, and 8.84%, respectively.

### 2.3 Output characteristics of MRFC element

A theoretical model of a cylindrical MRFC element is shown in Fig. 5, where the driven cylinder radius is  $R_1$  and the driving cylinder radius is  $R_2$ . When the speed difference between the input and output is  $\Delta\omega$ , a torque produced is produced by the shear yielding stress of the MRF.



(a) Two-dimensional structure diagram of MRFC



(b) Three-dimensional model of MRFC

Fig. 2 Assembly of the MRFC

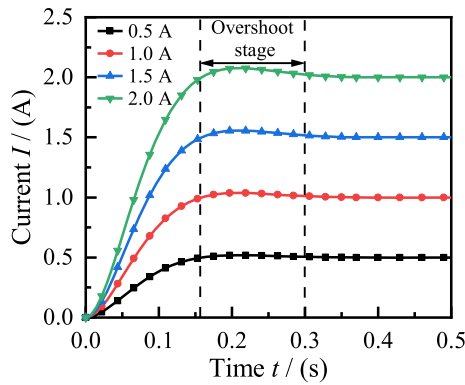


**Fig. 4** Current response curve

In the magnetic field, the MRF transforms from a Newtonian fluid to a Bingham fluid with a high viscosity and a low fluidity. Its intrinsic structure model is expressed as [27]:

$$\tau = \tau_{(H)} + \eta \dot{\gamma} \tag{3}$$

where  $\tau_{(H)}$  is the dynamic yield stress of the MRF,  $\eta$  is the zero-field viscosity of the MRF, and  $\dot{\gamma}$  is the shear strain rate of the MRF. In a magnetic field, the MRF solidifies and the internal magnetic particles form a chain-like structure. The torsional stiffness and damping factor produced by the MRFC are related to the degree of curing of the MRF at different currents. At the different currents, the magnetic flux density of the MRF is related to the magnetic field intensity as follows:

$$B = \mu_0 \mu_r H \tag{4}$$

where  $\mu_0$  is the vacuum magnetic permeability of the MRF and  $\mu_r$  is the relative magnetic permeability of the MRF, and it is related to the volume fraction of the MRF. The MRF is assumed to have a working gap in

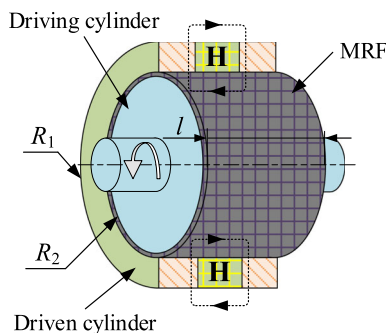


**Fig. 5** Theoretical model of MRFC

the entire yield shear flow in the magnetic field. Considering the MRF working gap length is  $l$ , the torque transmitted by the MRF is expressed as [28]:

$$M = \frac{4\pi R_1^2 R_2^2}{R_1^2 - R_2^2} \left( \tau_{(H)} l \ln \left( \frac{R_2}{R_1} \right) + \eta l_e \Delta \omega \right) \tag{5}$$

where the MRF effective working gap length is  $l_e$ .

2.4 Dynamic characteristics of MRFC element

In different currents, the MRF gap with different magnetic field intensities and the stiffness of the MRF vary with the degree of solidification as it changes from a Newtonian to a non-Newtonian fluid. The degree of curing of the MRF at a current is mainly related to the relative shear modulus,  $E_M$ , at this current. Thus, the relationship between the MRF relative shear modulus,  $E_M$ , and the current is expressed as [29]:

$$E_M = E' (1 + \lambda I) = E' + IE'' \tag{6}$$

where  $E'$  is the storage modulus and  $E''$  is the loss modulus,  $\lambda$  is the loss factor.  $E'$  is expressed as a cubic function of the magnetic field intensity as follows:

$$E' = \begin{cases} \rho \mu_0 H^2 & (H \leq 7.95 \text{ kA/m}) \\ 3\rho \mu_0 B_s H^{\frac{3}{2}} & (7.95 \text{ kA/m} \leq H \leq 477.4 \text{ kA/m}) \\ \frac{24\sqrt{5}}{625} B_s \rho \mu_0 & (H > 477.4 \text{ kA/m}) \end{cases} \tag{7}$$

where  $\rho$  is the volume fraction of the MRF,  $B_s$  is the magnetization intensity of the MRF at saturation magnetic. It is generally calculated using an empirical formula expressed as follows:

$$\lambda = \begin{cases} 0.22 + 21.3H^2 - 94.8H^3 & (0 \leq H \leq H_1) \\ 0.34 + 0.53H - 1.77H^2 & (H_1 < H \leq H_2) \end{cases} \tag{8}$$

where  $H_1 = 119.3\text{kA/m}$ ,  $H_2 = 238.7\text{kA/m}$ . The Loss modulus,  $E''$ , can be expressed as:

$$E'' = \lambda E' \tag{9}$$

when the initial shear modulus is  $E_0 = 3.5\text{kPa}$  (without a magnetic field), Eqs. (7) and (8), combined to yield the variation laws of relative shear modulus  $E_M$  versus current  $I$  and magnetic field intensity  $H$ . The results are shown in Fig. 6.

At a given magnetic field intensity, the torsional stiffness coefficient,  $k_M$ , of the MRF is a complex number and calculated as [30]:

$$k_M = \frac{4\pi l R_1^2 R_2^2 E_M}{R_1^2 - R_2^2} \tag{10}$$

The torsional damping coefficient,  $c_M$ , is calculated as

$$c_M = \zeta_M C_c = 2\zeta_M \omega_n J_M \tag{11}$$

where  $J_M$  is the rotational inertia of the MRFC,  $C_c$  is the critical damping coefficient of the MRF,  $\omega_n$  is the angular frequency, and  $\zeta_M$  is the damping ratio, which is calculated as

$$\zeta_M = \frac{\lambda}{2} \tag{12}$$

The dynamic mode of the MRFC element is

$$M_M \ddot{X}_M + C_M \dot{X}_M + K_M X_M = 0 \tag{13}$$

where  $C_M$  and  $K_M$  are the damping and stiffness matrices of the MRFC element, respectively. The damping matrix,  $C_M$ , has the same form as the stiffness matrix,  $K_M$ .  $M_M$  and  $X_M$  are the mass and displacement matrices, respectively. Corresponding to the MRFC element, they are expressed as

$$\begin{cases} K_M = \begin{bmatrix} 0 & 0 & 0 & 0 & 0 \\ 0 & 0 & 0 & 0 & 0 \\ 0 & 0 & k_m & 0 & -k_m \\ 0 & 0 & 0 & 0 & 0 \\ 0 & 0 & -k_m & 0 & k_m \end{bmatrix} \\ X_M = [0 \ 0 \ 0 \ 0 \ x_m]^T \\ M_M = \text{diag}[0 \ 0 \ 0 \ 0 \ m_m] \end{cases} \tag{14}$$

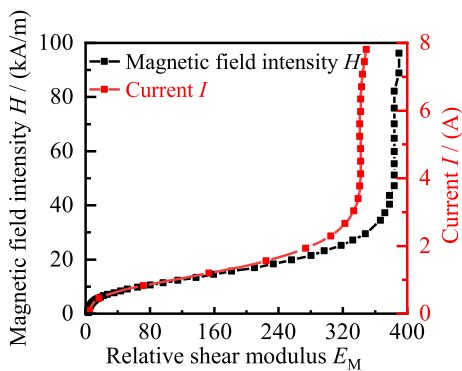


**Fig. 6** Relative shear modulus versus current and magnetic field intensity

### 3 Mechanical–electromagnetic coupled dynamics model

An MGTS, as shown in Fig. 1, consists of a drive motor, coupling, gear transmission system, and loading device. According to its structural features, the MGTS is divided into drive motor, shafting, gear meshing, bearing, connecting, and MRFC elements. In this study, an induction motor with a rate power of 15 kW is used as the drive motor, and its key parameters are listed in Table 1. The model of the drive motor is established in the d–q coordinate system, and its detailed description is available in Reference [31].

#### 3.1 Dynamic model of shafting element

The shafting element is described by a two-node (nodes  $j$  and  $j + 1$ ) Timoshenko beam, as shown in Fig. 7, where each node has six degrees of freedom. These are translational and rotational displacements along and around the  $x$ ,  $y$ , and  $z$  axes, respectively.

The displacement of the two-node shafting element in the  $x$ – $y$ – $z$  spatial coordinate system is expressed as [32]

$$X_S = \left( x_j, y_j, z_j, \theta_{x_j}, \theta_{y_j}, \theta_{z_j}, x_{j+1}, y_{j+1}, z_{j+1}, \theta_{x_{j+1}}, \theta_{y_{j+1}}, \theta_{z_{j+1}} \right)^T \tag{15}$$

where  $x_j, y_j, z_j$  and  $x_{j+1}, y_{j+1}, z_{j+1}$  are the translation displacements of nodes  $j$  and  $j + 1$  in the three directions of the  $x$ – $y$ – $z$  rectangular coordinate system, respectively.  $\theta_{x_j}, \theta_{y_j}, \theta_{z_j}$  and  $\theta_{x_{j+1}}, \theta_{y_{j+1}}, \theta_{z_{j+1}}$  are the rotational angular displacements of nodes  $j$  and  $j + 1$  in the three directions of the  $x$ – $y$ – $z$  rectangular coordinate system, respectively. The dynamic model of the shafting element is expressed as

**Table 1** Key parameters of drive motor

	Stator	Rotor
Resistance $R$	0.28820 $\Omega$	0.14191 $\Omega$
Rated speed $\omega$	–	1460 rpm
Voltage $V$	380 V	–
Current $I$	30.1 A	30.1 A
Leakage inductance $H$	0.00342 H	0.00342 H
Rotational inertia $J$	–	0.0918 kg·m <sup>2</sup>
Magnetizing inductance $H$	0.05773 H	0.05773 H



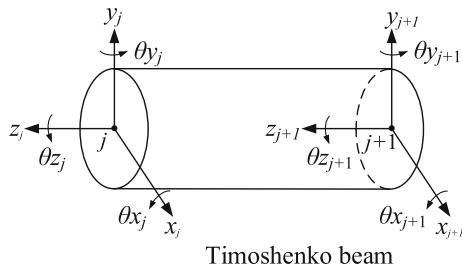


**Fig. 7** Dynamic model of shafting element

$$M_S \ddot{X}_S + (\Omega G_S + C_S) \dot{X}_S + K_S X_S = F_S \tag{16}$$

where  $M_S$  is the mass matrix,  $K_S$  is the stiffness matrix,  $\Omega$  is the spin speed,  $G_S$  is the gyroscopic matrix,  $C_S$  is the damping matrix of Timoshenko beam element, respectively. And  $F_S$  is the excitation force acting on nodes  $j$  and  $j + 1$  of the shafting element, respectively. Gyroscopic matrix  $G_S$ , continuous mass matrix  $M_S$  and stiffness matrix  $K_S$  can be expressed as

$$\begin{cases} M_S = \rho A a \begin{bmatrix} m_{s1} & m_{s2} \\ m_{s3} & m_{s4} \end{bmatrix} \\ G_S = 2\rho A a \begin{bmatrix} g_{s1} & g_{s2} \\ g_{s3} & g_{s4} \end{bmatrix} \\ K_S = \begin{bmatrix} k_{s1} & k_{s2} \\ k_{s3} & k_{s4} \end{bmatrix} \end{cases} \tag{17}$$

where  $\rho$  is the density of the shaft material,  $A$  is the cross-sectional area of the beam element ( $m^2$ ),  $a$  is the length of the beam element ( $m$ ).  $m_{s1}$ ,  $m_{s2}$ ,  $m_{s3}$ , and  $m_{s4}$  can be expressed as [33]

$$\begin{cases} m_{s1} = \begin{bmatrix} a_1 & 0 & 0 & 0 & a_3 & 0 \\ 0 & a_1 & 0 & -a_3 & 0 & 0 \\ 0 & 0 & 1/3 & 0 & 0 & 0 \\ 0 & -a_3 & 0 & a_5 & 0 & 0 \\ a_3 & 0 & 0 & 0 & a_5 & 0 \\ 0 & 0 & 0 & 0 & 0 & j/(3A) \end{bmatrix} \\ m_{s2} = \begin{bmatrix} a_2 & 0 & 0 & 0 & a_4 & 0 \\ 0 & a_2 & 0 & -a_4 & 0 & 0 \\ 0 & 0 & 1/6 & 0 & 0 & 0 \\ 0 & a_2 & 0 & a_6 & 0 & 0 \\ -a_4 & 0 & 0 & 0 & a_6 & 0 \\ 0 & 0 & 0 & 0 & 0 & j/(6A) \end{bmatrix} \\ m_{s3} = m_{s2} \\ m_{s4} = m_{s1} \end{cases} \tag{18}$$

$$\begin{cases} a_1 = \frac{13}{35} + \frac{7}{10}\zeta + \frac{1}{3}\zeta^2 + \frac{6}{5}\left(\frac{r_s}{a}\right)^2, \\ a_2 = \frac{9}{70} + \frac{3}{10}\zeta + \frac{1}{6}\zeta^2 - \frac{6}{5}\left(\frac{r_s}{a}\right)^2, \left(\zeta = \frac{12EP}{G_m A n a^2}\right) \\ a_3 = \frac{\left[\frac{11}{210} + \frac{11}{120}\zeta + \frac{1}{24}\zeta^2 + \left(\frac{1}{10} - \frac{1}{2}\zeta\right)\left(\frac{r_s}{a}\right)^2\right] a}{(1+\zeta)^2}, \\ a_4 = \frac{\left[\frac{13}{420} + \frac{3}{40}\zeta + \frac{1}{24}\zeta^2 - \left(\frac{1}{10} - \frac{1}{2}\zeta\right)\left(\frac{r_s}{a}\right)^2\right] a}{(1+\zeta)^2} \\ a_5 = \frac{\left[\frac{1}{105} + \frac{1}{60}\zeta + \frac{1}{120}\zeta^2 + \left(\frac{2}{15} + \frac{1}{6}\zeta + \frac{1}{3}\zeta^2\right)\left(\frac{r_s}{a}\right)^2\right] a^2}{(1+\zeta)^2} \\ a_6 = \frac{\left[\frac{1}{140} + \frac{1}{60}\zeta + \frac{1}{120}\zeta^2 + \left(\frac{1}{30} + \frac{1}{6}\zeta - \frac{1}{6}\zeta^2\right)\left(\frac{r_s}{a}\right)^2\right] a^2}{(1+\zeta)^2} \end{cases} \tag{19}$$

where  $\zeta$  is the shear influence factor,  $E$  is the elastic modulus of the shaft material ( $Pa$ ),  $P$  is the moment of inertia of a section ( $m^4$ ),  $n$  is the section influence coefficient,  $G_m$  is the shear elastic modulus of the shaft material ( $Pa$ ) and  $r_s$  is radius of gyration.  $g_{s1}$ ,  $g_{s2}$ ,  $g_{s3}$ , and  $g_{s4}$  can be expressed as

$$\begin{cases} g_{s1} = \begin{bmatrix} 0 & b_1 & 0 & b_2 & 0 & 0 \\ -b_1 & 0 & 0 & 0 & b_2 & 0 \\ 0 & 0 & 0 & 0 & 0 & 0 \\ -b_2 & 0 & 0 & 0 & b_3 & 0 \\ 0 & -b_2 & 0 & -b_3 & 0 & 0 \\ 0 & 0 & 0 & 0 & 0 & 0 \end{bmatrix} \\ g_{s2} = \begin{bmatrix} 0 & -b_1 & 0 & b_2 & 0 & 0 \\ b_1 & 0 & 0 & 0 & b_2 & 0 \\ 0 & 0 & 0 & 0 & 0 & 0 \\ b_2 & 0 & 0 & 0 & b_4 & 0 \\ 0 & b_2 & 0 & -b_4 & 0 & 0 \\ 0 & 0 & 0 & 0 & 0 & 0 \end{bmatrix} \\ g_{s3} = \begin{bmatrix} 0 & -b_1 & 0 & -b_2 & 0 & 0 \\ b_1 & 0 & 0 & 0 & -b_2 & 0 \\ 0 & 0 & 0 & 0 & 0 & 0 \\ -b_2 & 0 & 0 & 0 & b_4 & 0 \\ 0 & -b_2 & 0 & -b_4 & 0 & 0 \\ 0 & 0 & 0 & 0 & 0 & 0 \end{bmatrix} \\ g_{s4} = \begin{bmatrix} 0 & b_1 & 0 & -b_2 & 0 & 0 \\ -b_1 & 0 & 0 & 0 & -b_2 & 0 \\ 0 & 0 & 0 & 0 & 0 & 0 \\ b_2 & 0 & 0 & 0 & b_3 & 0 \\ 0 & b_2 & 0 & -b_3 & 0 & 0 \\ 0 & 0 & 0 & 0 & 0 & 0 \end{bmatrix} \end{cases} \tag{20}$$

$$\begin{cases} b_1 = \frac{6r_s^2}{5a^2(1+\zeta)^2}, b_2 = \frac{(5\zeta-1)r_s^2}{10a(1+\zeta)^2}, \\ b_3 = \frac{(10\zeta^2+5\zeta+4)r_s^2}{30(1+\zeta)^2}, b_4 = \frac{(5\zeta^2-5\zeta-1)r_s^2}{30(1+\zeta)^2} \end{cases} \quad (21)$$

where  $k_{s1}, k_{s2}, k_{s3}$ , and  $k_{s4}$  can be expressed as

$$\begin{cases} k_{s1} = \begin{bmatrix} c_1 & 0 & 0 & 0 & c_3 & 0 \\ 0 & c_2 & 0 & -c_4 & 0 & 0 \\ 0 & 0 & (AE)/a & 0 & 0 & 0 \\ 0 & -c_3 & 0 & c_5 & 0 & 0 \\ c_4 & 0 & 0 & 0 & c_6 & 0 \\ 0 & 0 & 0 & 0 & 0 & (Gj)/a \end{bmatrix} & k_{s2} = \begin{bmatrix} -c_1 & 0 & 0 & 0 & c_3 & 0 \\ 0 & -c_2 & 0 & -c_4 & 0 & 0 \\ 0 & 0 & -(AE)/a & 0 & 0 & 0 \\ 0 & c_3 & 0 & c_7 & 0 & 0 \\ -c_4 & 0 & 0 & 0 & c_8 & 0 \\ 0 & 0 & 0 & 0 & 0 & -(Gj)/a \end{bmatrix} \\ k_{s3} = \begin{bmatrix} -c_1 & 0 & 0 & 0 & -c_3 & 0 \\ 0 & -c_2 & 0 & c_4 & 0 & 0 \\ 0 & 0 & -(AE)/a & 0 & 0 & 0 \\ 0 & -c_4 & 0 & c_7 & 0 & 0 \\ c_3 & 0 & 0 & 0 & c_8 & 0 \\ 0 & 0 & 0 & 0 & 0 & -(Gj)/a \end{bmatrix} & k_{s4} = \begin{bmatrix} c_1 & 0 & 0 & 0 & -c_3 & 0 \\ 0 & c_2 & 0 & c_4 & 0 & 0 \\ 0 & 0 & (AE)/a & 0 & 0 & 0 \\ 0 & c_3 & 0 & c_5 & 0 & 0 \\ -c_4 & 0 & 0 & 0 & c_6 & 0 \\ 0 & 0 & 0 & 0 & 0 & (Gj)/a \end{bmatrix} \end{cases} \quad (22)$$

$$\begin{cases} c_1 = c_2 = \frac{12EP}{a^3(1+\zeta)}, c_3 = c_4 = \frac{6EP}{a^2(1+\zeta)} \\ c_5 = c_6 = \frac{(4+\zeta)EP}{a(1+\zeta)}, c_7 = c_8 = \frac{(2-\zeta)EP}{a(1+\zeta)} \end{cases} \quad (23)$$

The damping matrix  $C_S$  of the Timoshenko beam element is calculated using the Rayleigh damping,  $C_S$ , as follows:

$$C_S = pM_S + qK_S \quad (24)$$

where  $p$  and  $q$  are the mass and stiffness scaling coefficients in Rayleigh damping, respectively, and are expressed as

$$\begin{cases} p = \frac{2\left(\frac{\zeta_2}{\omega_2} - \frac{\zeta_1}{\omega_1}\right)}{\left(\frac{1}{\omega_2^2} - \frac{2}{\omega_1^2}\right)}, q = \frac{2(\zeta_2\omega_2 - \zeta_1\omega_1)}{(\omega_2^2 - \omega_1^2)} \end{cases} \quad (25)$$

where  $\zeta_1$  and  $\zeta_2$  are damping coefficients and  $\omega_1$  and  $\omega_2$  are the first two orders of the intrinsic frequency of the system.

### 3.2 Dynamic model of gear meshing element

The dynamic model of the gear meshing element is shown in Fig. 8, and the key parameters of the gear pair are listed in Table 2. In Fig. 8,  $\alpha$  is the pressure angle,  $\gamma$  is the angle between the helical gear end meshing line and the  $y$  axis positive direction, and  $\beta_b$  is the helical angle.  $r_1$  and  $r_2$  are the base radii of the

driving and driven gears (positive value for dextrorotation and negative value for levorotation), respectively.  $K_G$  and  $C_G$  are the meshing stiffness and damping, respectively.

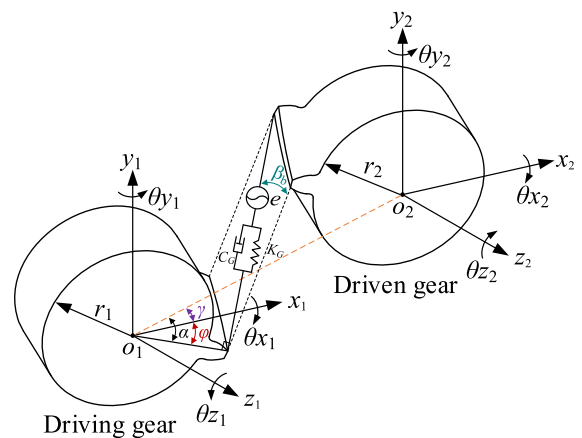


Fig. 8 Dynamic model of gear meshing element

**Table 2** Key parameters of helical gears

	Driving gear	Driven gear
Module	2 mm	2 mm
Tooth number	29	180
Width	50 mm	45 mm
Pressure angle	20°	20°
Helix angle	15°	15°
Mass	1.03 kg	24.06 kg
Moment of inertia	$4.31 \times 10^{-4}$ kg/m <sup>2</sup>	0.41 kg/m <sup>2</sup>
Supporting stiffness	$6.81 \times 10^7$ N·m <sup>-1</sup>	$7.87 \times 10^7$ N·m <sup>-1</sup>
Revolving direction	Dextrorotation	Levorotation

In the generalized coordinate system,  $x$ - $y$ - $z$ , the displacement column vector of the gear meshing element is expressed as [34]

$$X_G = [x_1, y_1, z_1, \theta_{x1}, \theta_{y1}, \theta_{z1}, x_2, y_2, z_2, \theta_{x2}, \theta_{y2}, \theta_{z2}]^T \tag{26}$$

where  $x_{xi}, y_{xi}, z_{xi}$  denote the translational displacements of the driving gear along the  $x, y,$  and  $z$  axes, respectively.  $\theta_i (i = x_1, y_1, z_1$  and  $x_2, y_2, z_2)$  is the rotational angular displacement around the  $z$  axis.  $x_2, y_2, z_2$  denote the translational displacements of the driven gear along the  $x, y,$  and  $z$  axes, respectively.

The relative total deformation,  $\delta$ , is obtained by projecting the displacement of each gear along the direction of the meshing line, and it is expressed as

$$\delta = V_G(X_G - e) \tag{27}$$

where  $e$  is the transmission error and  $V_G$  is the meshing matrix of the gear pair, which is expressed as

$$V_G = [\cos\beta_b \sin\varphi, \pm \cos\varphi \cos\beta_b, \sin\beta_b, \mp r_1 \sin\beta_b \sin\varphi, -r_1 \cos\varphi \sin\beta_b, \pm r_1 \cos\beta_b, -\cos\beta_b \sin\varphi, \mp \cos\varphi \cos\beta_b, -\sin\beta_b, \mp r_2 \sin\beta_b \sin\varphi, -r_2 \cos\varphi \sin\beta_b, \pm r_2 \cos\beta_b] \tag{28}$$

where “+” indicates counter-clockwise rotation of the driving gear and angle  $\varphi = \alpha - \gamma$ . “-” indicates clockwise rotation of the driving gear and angle  $\varphi = \alpha + \gamma$ . The dynamic equations for the helical gear meshing unit are expressed as [35]

$$\left\{ \begin{aligned} m_1 \ddot{x}_1 + (c_m \dot{\delta} + k_m \delta) \cos\beta_b \sin\varphi &= -f_s \cos\beta_b \sin\varphi \\ m_1 \ddot{y}_1 \pm (c_m \dot{\delta} + k_m \delta) \cos\beta_b \cos\varphi &= \mp f_s \cos\beta_b \cos\varphi \\ m_1 \ddot{z}_1 + (c_m \dot{\delta} + k_m \delta) \sin\beta_b &= -f_s \sin\beta_b \\ I_{x1} \ddot{\theta}_{x1} + I_{z1} \Omega_1 \dot{\theta}_{y1} &= 0 \\ I_{y1} \ddot{\theta}_{y1} - I_{z1} \Omega_1 \dot{\theta}_{x1} &= 0 \\ I_{z1} \ddot{\theta}_{z1} \pm (c_m \dot{\delta} + k_m \delta) r_1 \cos\beta_b &= \mp f_s r_1 \cos\beta_b \\ m_2 \ddot{x}_2 - (c_m \dot{\delta} + k_m \delta) \cos\beta_b \sin\varphi &= f_s \cos\beta_b \sin\varphi \\ m_2 \ddot{y}_2 \mp (c_m \dot{\delta} + k_m \delta) \cos\beta_b \cos\varphi &= \pm f_s \cos\beta_b \cos\varphi \\ m_2 \ddot{z}_2 - (c_m \dot{\delta} + k_m \delta) \sin\beta_b &= f_s \sin\beta_b \\ I_{x2} \ddot{\theta}_{x2} + I_{z2} \Omega_2 \dot{\theta}_{y2} &= 0 \\ I_{x2} \ddot{\theta}_{x2} - I_{z2} \Omega_2 \dot{\theta}_{x2} &= 0 \\ I_{z2} \ddot{\theta}_{z2} \pm (c_m \dot{\delta} + k_m \delta) r_2 \cos\beta_b &= \mp f_s r_2 \cos\beta_b \end{aligned} \right. \tag{29}$$

where  $m_1$  and  $m_2$  are the masses of the driving and driven gears, respectively,  $I_{x1}, I_{y1}, I_{z1}$  and  $I_{x2}, I_{y2}, I_{z2}$  are the rotational inertia of the driving and driven gears around the  $x$ - $y$ - $z$  axis, respectively,  $\Omega_1$  and  $\Omega_2$  is rotation angular speed of the driving and driven gears, respectively,  $f_s$  is the normal force of the helical gear pair,  $k_m$  is the helical gear pair meshing stiffness,  $c_m$  is the helical gear pair meshing damping,  $K_G$  is the stiffness matrix of helical gear meshing element,  $C_G$  is the damping matrix of the helical gear meshing element,  $G_G$  is the gyroscopic matrix of helical gear meshing element, and  $M_G$  is the mass matrix of helical gear meshing element. These matrices are expressed as

$$\left\{ \begin{aligned} K_G &= k_m V_G^T V_G = k_m \begin{bmatrix} k_{g1} & k_{g2} \\ k_{g3} & k_{g4} \end{bmatrix} \\ M_G &= \text{diag}\{m_1, m_1, m_1, I_{x1}, I_{y1}, I_{z1}, m_2, m_2, m_2, I_{x2}, I_{y2}, I_{z2}\} \\ C_G &= c_m \begin{bmatrix} k_{g1} & k_{g2} \\ k_{g3} & k_{g4} \end{bmatrix} \\ G_G &= \begin{bmatrix} g_{g1} & g_{g2} \\ g_{g3} & g_{g4} \end{bmatrix} \end{aligned} \right. \tag{30}$$

where  $k_{g1}, k_{g2}, k_{g3},$  and  $k_{g4}$  are obtained based on Reference [36].  $g_{g1}, g_{g2}, g_{g3},$  and  $g_{g4}$  can be expressed as

$$\left\{ \begin{array}{l} g_{g1} = \begin{bmatrix} 0 & 0 & 0 & 0 & 0 & 0 \\ 0 & 0 & 0 & 0 & 0 & 0 \\ 0 & 0 & 0 & 0 & 0 & 0 \\ 0 & 0 & 0 & 0 & I_{z1}\Omega_1 & 0 \\ 0 & 0 & 0 & -I_{z1}\Omega_1 & 0 & 0 \\ 0 & 0 & 0 & 0 & 0 & 0 \end{bmatrix} \\ g_{g2} = \begin{bmatrix} 0 & 0 & 0 & 0 & 0 & 0 \\ 0 & 0 & 0 & 0 & 0 & 0 \\ 0 & 0 & 0 & 0 & 0 & 0 \\ 0 & 0 & 0 & 0 & 0 & 0 \\ 0 & 0 & 0 & 0 & 0 & 0 \\ 0 & 0 & 0 & 0 & 0 & 0 \end{bmatrix} \\ g_{g3} = \begin{bmatrix} 0 & 0 & 0 & 0 & 0 & 0 \\ 0 & 0 & 0 & 0 & 0 & 0 \\ 0 & 0 & 0 & 0 & 0 & 0 \\ 0 & 0 & 0 & 0 & 0 & 0 \\ 0 & 0 & 0 & 0 & 0 & 0 \\ 0 & 0 & 0 & 0 & 0 & 0 \end{bmatrix} \\ g_{g4} = \begin{bmatrix} 0 & 0 & 0 & 0 & 0 & 0 \\ 0 & 0 & 0 & 0 & 0 & 0 \\ 0 & 0 & 0 & 0 & 0 & 0 \\ 0 & 0 & 0 & 0 & -I_{z2}\Omega_2 & 0 \\ 0 & 0 & 0 & -I_{z2}\Omega_2 & 0 & 0 \\ 0 & 0 & 0 & 0 & 0 & 0 \end{bmatrix} \end{array} \right. \quad (31)$$

Combining Eqs. (27)–(31), the dynamic model of the gear meshing element is expressed as

$$M_G \ddot{X}_G + (C_G + G_G)(\dot{X}_G - \dot{e}) + K_G(X_G - e) = F_G \quad (32)$$

where  $F_G$  is the external excitation force column vector, which is expressed as, respectively.

$$F_G = [0, 0, 0, -T_{in}, 0, 0, 0, -T_{load}]^T \quad (33)$$

### 3.3 Dynamic model of bearing element

The dynamic model of the bearing element is shown in Fig. 9, where  $K_B$  and  $C_B$  are the stiffness and damping matrices of the bearing support node,  $n$ , respectively. The damping matrix,  $C_B$ , has the same structural form as the stiffness matrix,  $K_B$ . Therefore, the dynamic model of the bearing element is described as

$$M_B \ddot{X}_B + C_B \dot{X}_B + K_B X_B = 0 \quad (34)$$

where  $M_B$  and  $X_B$  are the mass matrix and displacement column vector of node  $n$ , respectively.  $K_B$  is expressed as:

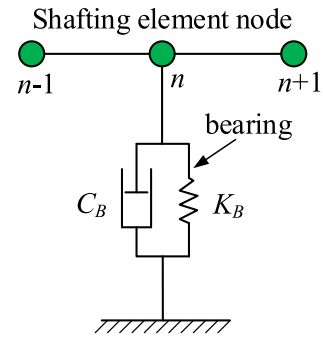


Fig. 9 Dynamic model of bearing element

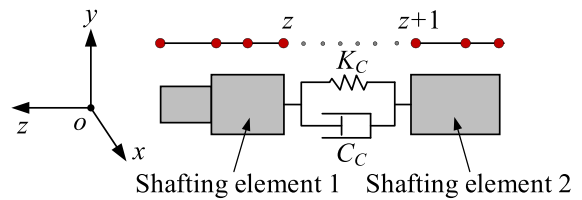


Fig. 10 Dynamic model of connecting element

$$K_B = \begin{bmatrix} k_{xx} & k_{xy} & k_{xz} & k_{x\theta x} & k_{x\theta y} & 0 \\ k_{yx} & k_{yy} & k_{yz} & k_{y\theta x} & k_{y\theta y} & 0 \\ k_{zx} & k_{zy} & k_{zz} & k_{z\theta x} & k_{z\theta y} & 0 \\ k_{\theta xx} & k_{\theta xy} & k_{\theta xz} & k_{\theta x\theta x} & k_{\theta x\theta y} & 0 \\ k_{\theta yx} & k_{\theta yy} & k_{\theta yz} & k_{\theta y\theta x} & k_{\theta y\theta y} & 0 \\ 0 & 0 & 0 & 0 & 0 & 0 \end{bmatrix} \quad (35)$$

where  $k_{xx}$  and  $k_{yy}$  are the radial stiffness,  $k_{zz}$  is the axial stiffness,  $k_{\theta x\theta x}$  and  $k_{\theta y\theta y}$  are the torsional stiffness of around the  $x$  and  $y$  axes, respectively.

### 3.4 Dynamic model of connecting element

The connecting element connects different mechanical components, such as shafting element 1 and shafting element 2, as shown in Fig. 10. The dynamic model of the connecting element is written as

$$M_C \ddot{X}_C + C_C \dot{X}_C + K_C X_C = 0 \quad (36)$$

where  $M_C$  is the mass matrix and  $X_C$  is the displacement column vector of connecting nodes  $z$  and  $z + 1$ ,  $C_C$  and  $K_C$  are the connecting stiffness and connecting damping matrices, respectively, and their specific forms are expressed as follows:

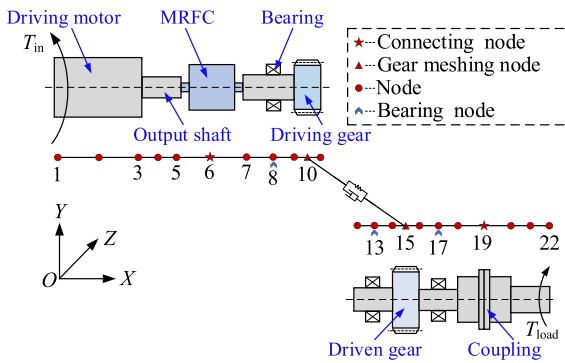


**Fig. 11** Mechanical–electromagnetic coupled dynamic model and node distribution diagram

$$\left\{ \begin{array}{l} C_c = \begin{bmatrix} c_x & & & & & \\ 0 & c_y & & & & \\ 0 & 0 & c_z & & & \\ 0 & 0 & 0 & c_{\theta x} & & \\ 0 & 0 & 0 & 0 & c_{\theta y} & \\ 0 & 0 & 0 & 0 & 0 & c_{\theta z} \end{bmatrix} \\ K_c = \begin{bmatrix} k_x & & & & & \\ 0 & k_y & & & & \\ 0 & 0 & k_z & & & \\ 0 & 0 & 0 & k_{\theta x} & & \\ 0 & 0 & 0 & 0 & k_{\theta y} & \\ 0 & 0 & 0 & 0 & 0 & k_{\theta z} \end{bmatrix} \\ M_c = \begin{bmatrix} m_z & 0 \\ 0 & m_{z+1} \end{bmatrix} \end{array} \right. \quad (37)$$

where  $m_z$  and  $m_{z+1}$  are the mass matrices of the connecting elements corresponding to node  $z$  and node  $z + 1$ , respectively.  $m_z$  and  $m_{z+1}$  are expressed as

$$\begin{cases} m_z = \text{diag}[m_z & m_z & m_z & I_{xz} & I_{yz} & I_{zz}] \\ m_{z+1} = \text{diag}[m_{z+1} & m_{z+1} & m_{z+1} & I_{xz+1} & I_{yz+1} & I_{zz+1}] \end{cases} \quad (38)$$

### 3.5 Dynamic model of electromechanical coupled dynamic model

The mechanical–electromagnetic coupled dynamic model and the node distribution diagram of the MGTS are shown in Fig. 11. Assembling the dynamics models of the different mechanical parts of the MGTS using the coupling method, the mechanical–electromagnetic coupled nonlinear dynamics model of the MGTS is obtained, as expressed in Eq. (39). Moreover, the driving torque ( $T_{in}$ ) of the drive motor is applied to node 4, and the load torque ( $T_{load}$ ) is applied to node 22.

$$M\ddot{X}(t) + (\Omega G + C)\dot{X}(t) + KX(t) = F(t) \quad (39)$$

where  $M$  is the whole mass matrix of the MGTS,  $K$  is the whole stiffness matrix of the MGTS,  $C$  is the whole damping matrix of the MGTS,  $G$  is the whole gyroscopic matrix of the MGTS,  $X(t)$  is the whole

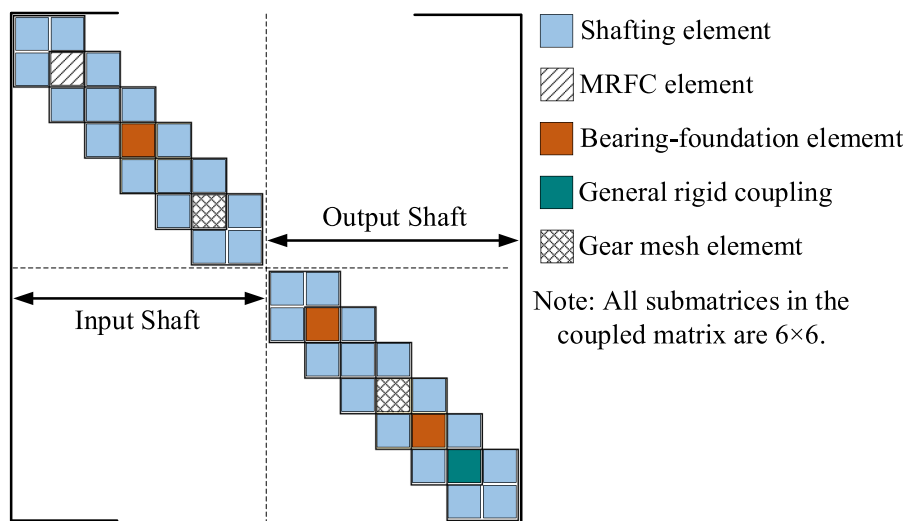


**Fig. 12** Structure of an entire assembled stiffness matrix of MGTS

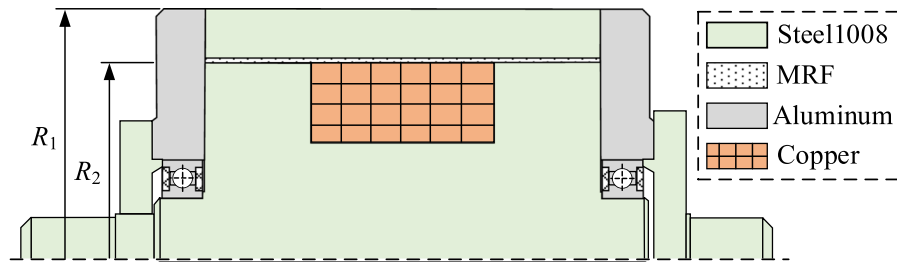


**Fig. 13** FEM model of MRFC

**Table 3** Structural dimensional parameters of MRFC (mm)

$R_1$	$R_2$	$l_e$
73	65	80

displacement vector of the MGTS, and  $F(t)$  is the system external load column vector.

Figure 12 shows the assembly arrangement of the MGTS global stiffness matrix. It involves establishing the dynamics equations of the different mechanical parts hierarchically using the finite unit method. Subsequently, assembling the stiffness matrix, the nonlinear dynamics problem of the continuous mass distribution system (MGTS) is transformed into a finite-degree of freedom system dynamics problem. The process of assembling the overall stiffness matrix of the transmission system is identical to that of assembling the finite element overall stiffness matrix in a conventional structural mechanics analysis. In the latter, the sub-matrices corresponding to each degree of freedom of the unit matrix are superimposed on the corresponding position of the overall matrix according to the correspondence between the local numbering of each unit node and the overall numbering of the system nodes in turn. The rotational angular displacements of each component of the MGTS in the  $x$  ( $\theta_x$ ) and  $y$  directions ( $\theta_y$ ) hardly change, and they are not considered in the study.

## 4 Result and discussion

### 4.1 Dynamic response of MRFC element

To more accurately analyze the rheological characteristics of the MRF under different currents, a two-dimensional axisymmetric finite element analysis model is established using the simplified model of the cylindrical MRFC element, which is shown in Fig. 2. As shown in Fig. 13, the magnetic field analysis of the MRFC element is conducted using the finite element method. The materials used for each part of the MRFC are shown in different colors in Fig. 13. Among them, the structural dimensional parameters of the cylindrical MRFC element are listed in Table 3.

To more accurately analyze the magnetic field characteristics of the MRFC, the nonlinear magnetic permeability of the different materials is considered in the magnetic field finite element analysis. Among them, the MRF is MRF-J01T provided by the Chongqing Institute of Materials and the base fluid is silicone oil. The material parameters of MRF-J01T are summarized in Table 4.

The magnetization and magnetic flux density versus shear yield stress curves of MRF-J01T are shown in Fig. 14(a). The relationship between the shear yield stress and the magnetic field intensity of MRF-J01T is approximated by fitting as follows:

$$\tau(H) = -0.001H^2 + 0.45H + 2.45 \quad (40)$$

**Table 4** Material parameters of MRF-J01T<sup>[37]</sup>

Working temperature $C$	Viscosity $\sigma$	Density $\rho$	Volume fraction $\varphi$	Particle size $d$
- 40 °C ~ 150 °C	0.38 Pa·s	2.65 g/cm <sup>3</sup>	25%	0.1 ~ 10 $\mu$ m

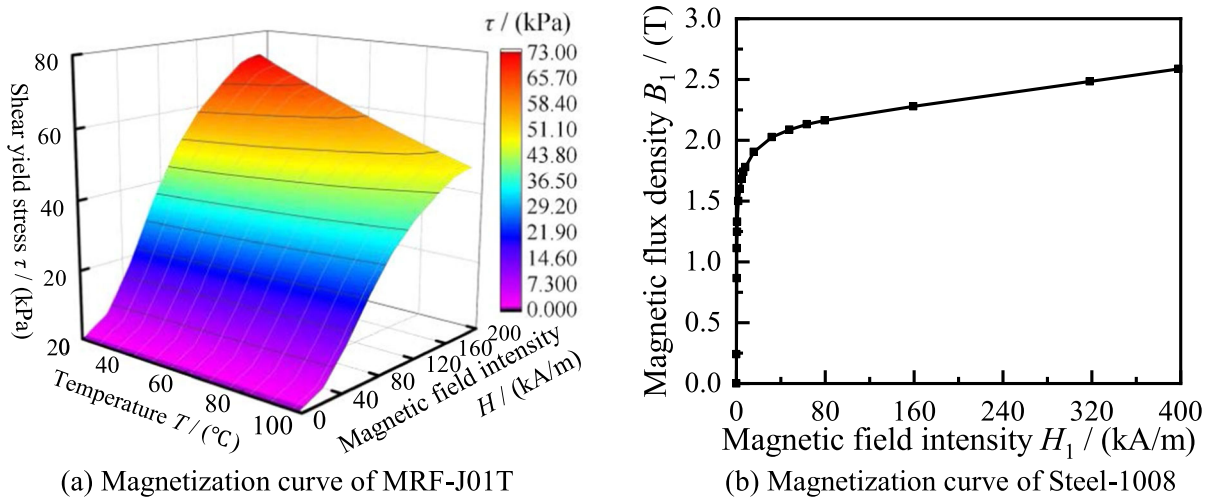


**Fig. 14** Magnetization curve of materials

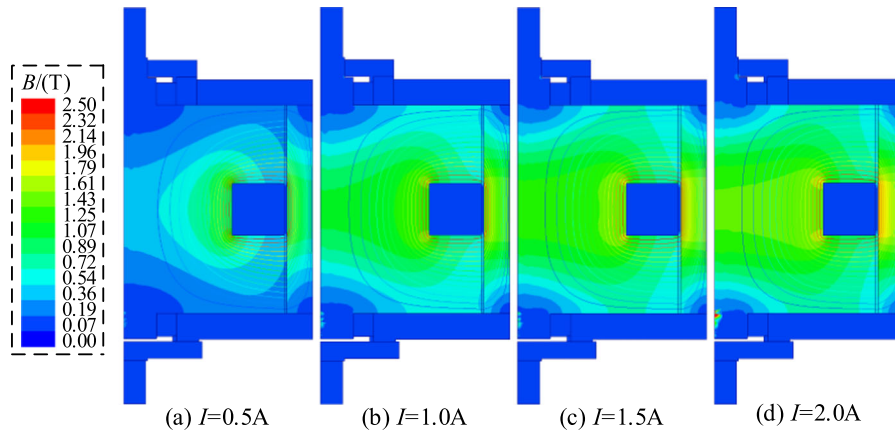


**Fig. 15** Cloud map of magnetic field distribution with different currents

The magnetization curve of Steel-1008 is shown in Fig. 14(b), and aluminum is a nonpermeable material with a relative magnetic permeability of approximately one.

In this study, an axisymmetric steady-state magnetic field is considered in the magnetic field analysis, and the materials of each part are set up as shown in Fig. 13. The number of turns of the excitation coil,  $N$ , is 400, and the area around the magnetic field analysis model is air with a relative magnetic permeability of one. The magnetic flux density and magnetic field line distribution clouds are calculated at different currents, and the results are shown at the same scale in Fig. 15(a)–(d). At any current, the magnetic lines are geometrically centered on the excitation coil and

gradually spread outward and form a closed circuit. The magnetic lines pass through the driving cylinder, driven cylinder, and MRF area vertically, in turn. The MRF produces the maximum shear yield stress after forming a chain along the magnetic line direction, indicating that the structure and material design of the MRFC are reasonable. With the increase in the coil current, the MRF shows magnetic saturation, and the magnetic flux density growth rate gradually decreases. When  $I = 0.5A$ , the average magnetic flux density of the MRF working gap is 0.24 T, and when the current gradually increases to 1.0 A, 1.5 A, and 2.0 A, the average magnetic flux density of the MRF working gap becomes 0.44 T, 0.62 T, and 0.7 T, respectively. Compared with the magnetic flux density at 0.5 A, the

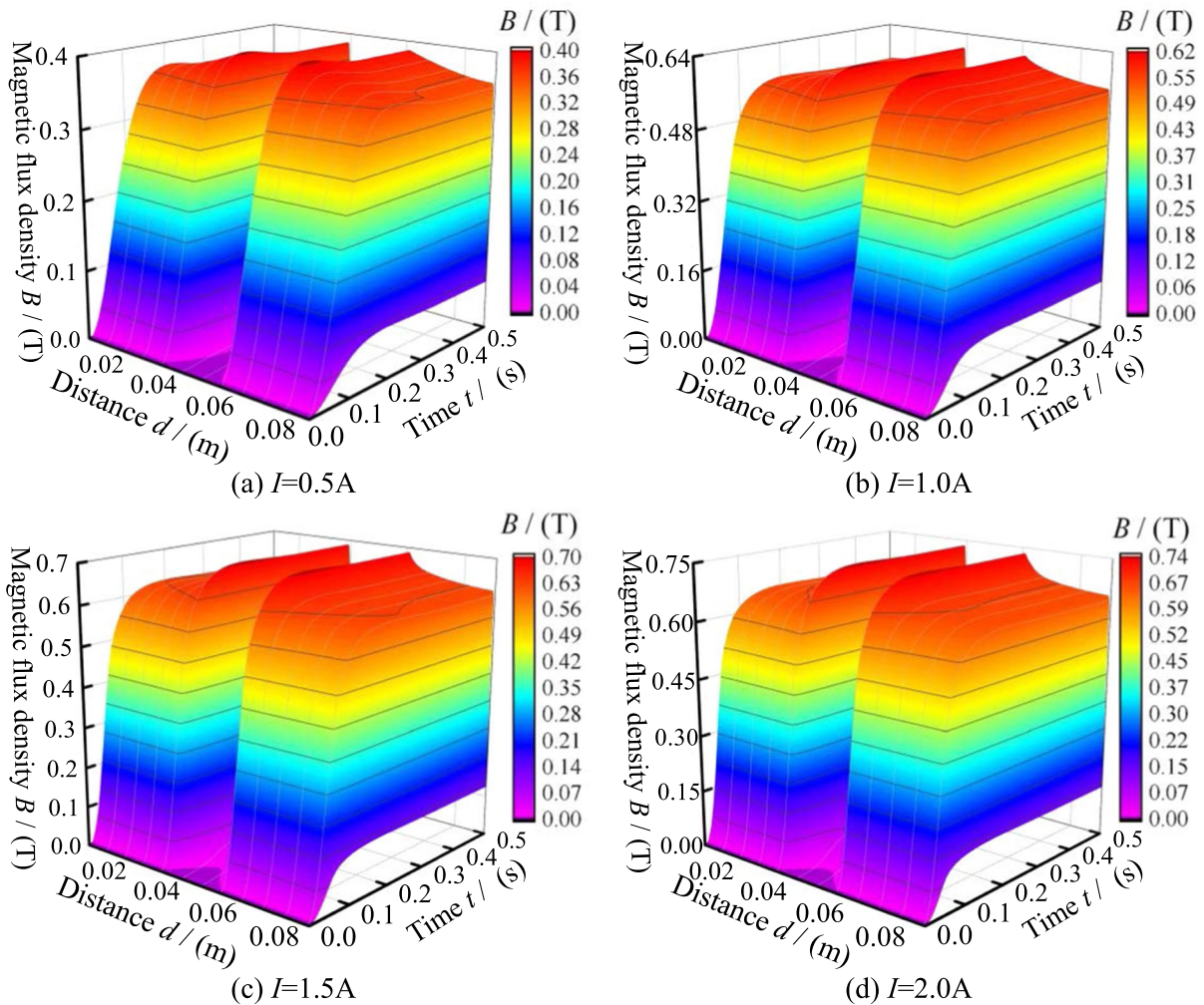


**Fig. 16** Axial magnetic flux density distribution versus different currents of MRF

magnetic flux density growth rates at the remaining currents are 83.3%, 158.3%, and 191.7%, respectively.

Meanwhile, when the coil is subjected to different currents, a magnetic field is generated and stabilized quickly. The variation laws of the magnetic flux density versus the current loading time for different distances of the MRF gap are shown in Fig. 16.

Figure 16 shows that under different currents, the trends of the magnetic induction intensity at different axial distances are consistent with those at different current loading times. The MRF working gap is divided into four parts along the axial direction according to the variation in the MRF magnetic flux density. In Part I, when axial distance  $d = 0\text{--}30$  mm,

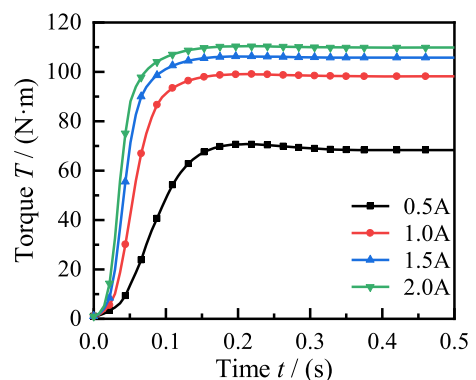


**Fig. 17** Current-torque response curve

the magnetic flux density increases rapidly along the



working gap and reaches the maximum value. In Part II, when axial distance  $d = 30\text{--}45$  mm, because the excitation coil is formed of a nonpermeable material, the magnetic flux density in the MRF gap gradually decreases along the working gap and reaches a minimum value. In Part III, when axial distance  $d = 45\text{--}60$  mm, the magnetic field density gradually increases again along the working gap and increases to a maximum value. In Part IV, when axial distance  $d = 60\text{--}90$  mm, the magnetic induction intensity decreases rapidly again along the working gap. The overshoot phenomenon during current loading causes the magnetic flux density at different distances of the MRF gap to first gradually increase and exceed the rated value and subsequently decrease to the rated value and stabilize. The magnetic flux density overshoot rate is linearly related to the current overshoot rate under the different currents.

At any current, the magnetic flux density of the MRF gap is symmetrically distributed, and the maximum magnetic flux densities are observed at the axial distances of  $d = 40$  mm and 60 mm, whereas the minimum one is noted at  $d = 45$  mm. When the current is 0.5 A, the maximum and minimum magnetic flux densities are 0.38 T and 0.06 T, respectively. When the currents are 1.0 A, 1.5 A, and 2.0 A, the maximum magnetic flux densities are 0.62 T, 0.68 T, and 0.74 T, respectively, and the minimum values are 0.08 T, 0.1 T, and 0.11 T, respectively. When the current loading time is increased to 0.15 s, the magnetic flux of each part tends to stabilize. The

relationship between the torque transferred by the MRFC element and the current is shown in Fig. 17.

The maximum torque that can be transmitted by the MRFC as a function of the current is shown in Fig. 17, and the transferred torque increases with increasing current. However, when the current loading time increases to a certain value, the torque tends to stabilize. The overshoot phenomenon during current loading causes the torque transferred by the MRF to also overshoot, and the maximum overshoot rates at the different currents are 20.5%, 15.7%, 12.4%, and 9.85%, respectively. When the current loading time is shorter than 0.29 s, the magnetic flux density of the MRF increases with increasing current, and the torque transferred by the MRFC element is also increased. When the current loading time exceeds 0.29 s, the MRF becomes magnetically saturated, the magnetic flux density ceases to increase, the torque stabilizes, and the maximum torque transferred by the MRFC element also tends to a constant value. To satisfy the needs of the MGTS to transfer torque, an appropriate current can be selected considering energy consumption, transmission efficiency, and shock strength. Three-dimensional surfaces of the torsional stiffness and damping coefficient of MRF with the current loading time for different currents are shown in Fig. 18(a) and (b), respectively.

The degree of curing of the MRF varies under the different currents, and the torsional stiffness and damping coefficient of the MRF increase nonlinearly with increasing current. Figure 18(a) and (b) shows

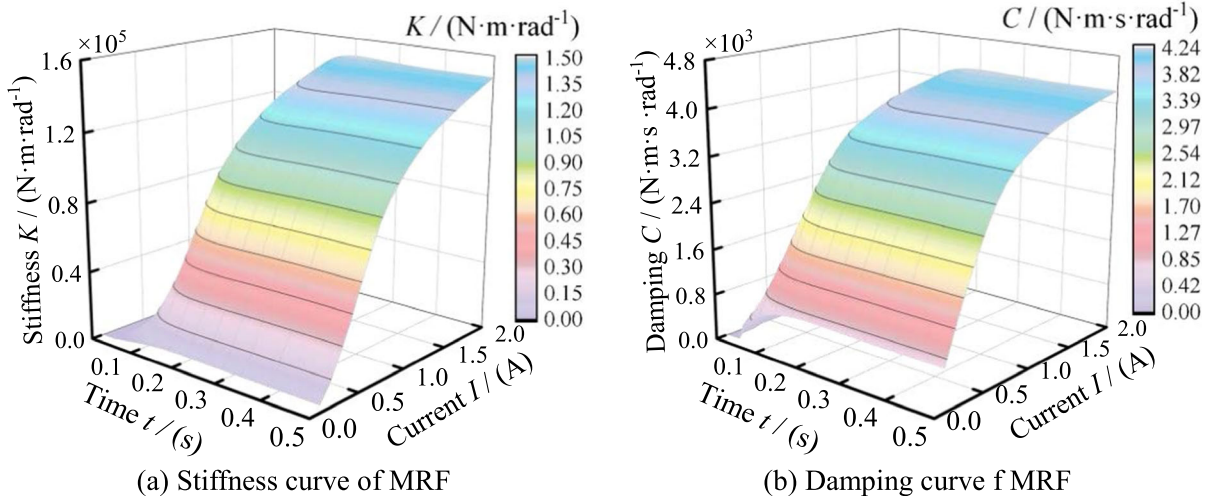
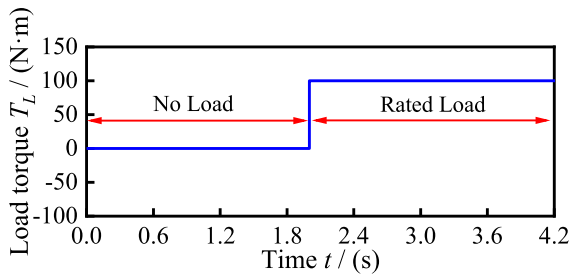


Fig. 18 Dynamic parameters of MRFC



**Fig. 19** Impact load

that the torsional stiffness and damping factor of the MRF increase with increasing current, and as the current loading time increases, these properties first rapidly increase and subsequently stabilize. The current loading process generates an overshoot, and when the current loading time is 0–0.29 s, the torsional stiffness and damping coefficient of the MRF gap first increase rapidly from a stable value to reach the maximum in a very short period. When the

current is 2.0 A, the magnetic field intensity and magnetically induced shear modulus of the MRF are the highest and the degree of curing of the MRF is the greatest. Both the torsional stiffness and damping factor reach their maximum values of  $1.51 \times 10^5$  (N·m·rad<sup>-1</sup>) and  $4.2 \times 10^3$  (N·m·s rad<sup>-1</sup>). When the current loading time exceeds 0.29 s, the torsional stiffness and damping factor of the MRF gap gradually decrease to stable values without any change. The MRF is in a non-Newtonian fluid state in the absence of a magnetic field, and it has a certain damping factor. Moreover, the MRFC can affect the stability of the transmission system when there is no current.

#### 4.2 Time-domain dynamic response of MGTS

The MGTS uses a single motor to apply shock loads, and the variation in the load versus the motor runtime is shown in Fig. 19. The completely applied load stage can be divided into two parts. Part I is from 0 s to 2.0 s,

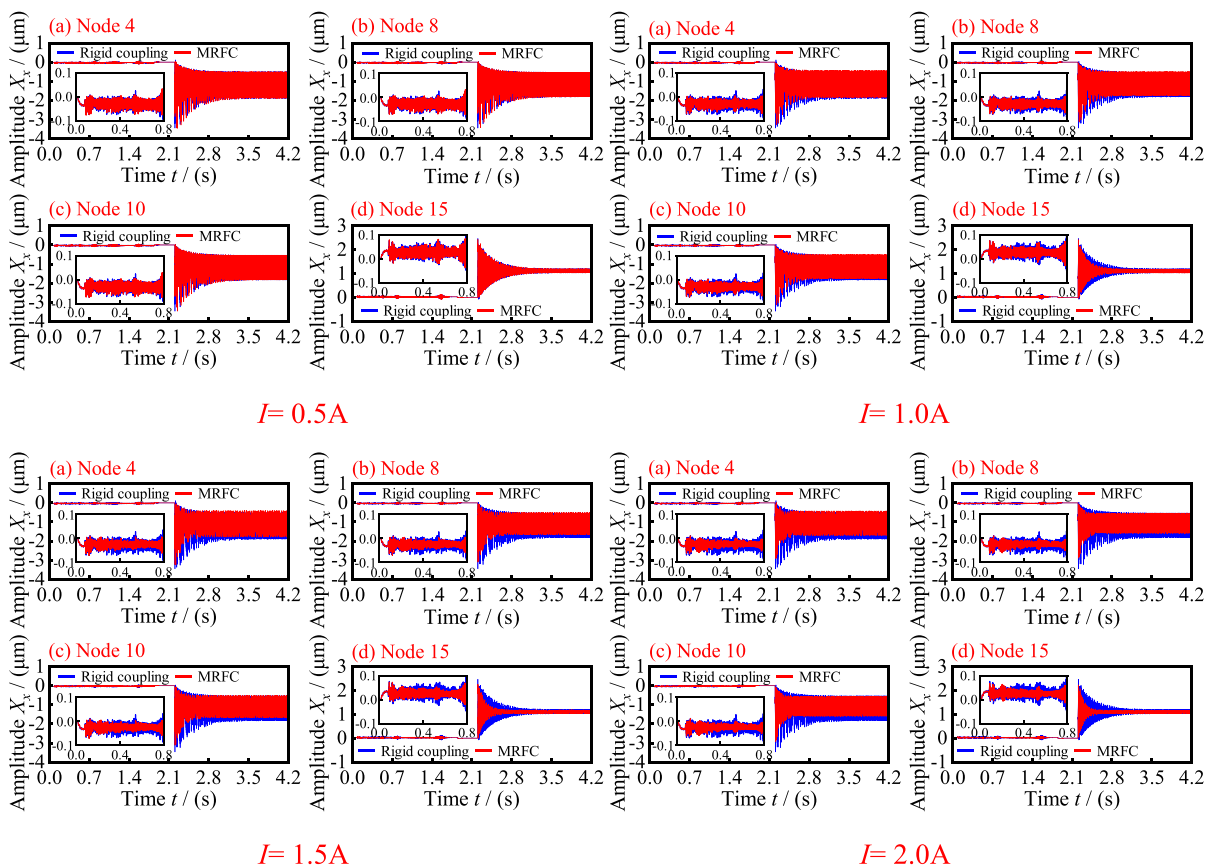


**Fig. 20** Displacement amplitude of four nodes in *x*-direction at different currents

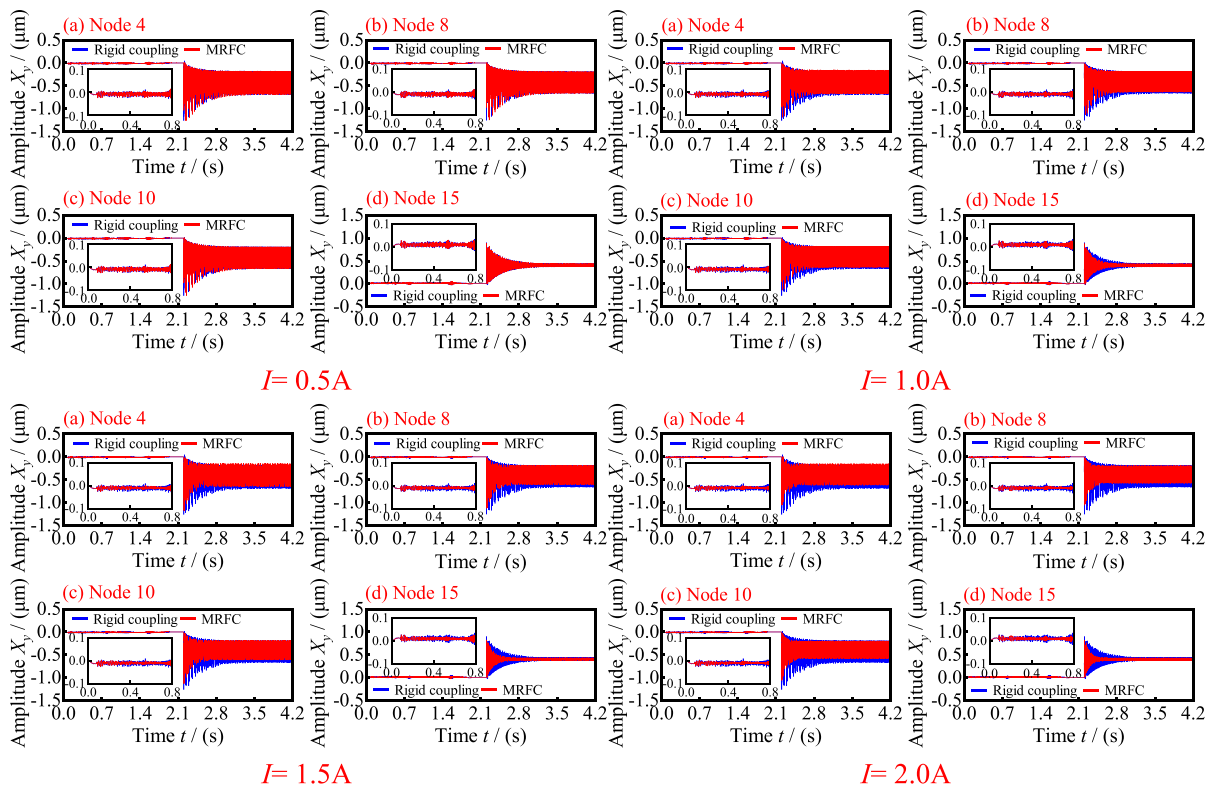


**Fig. 21** Displacement amplitude of four nodes in y-direction at different currents

which is the system no-load start-up phase, and in Part II, after 2.0 s, the load changes abruptly to 100 N·m, the load duration is 3.0 s, and the motor input speed is 1410 r/min.

To investigate the dynamic response variation of the MRF under different excitations, numerical simulations of the MGTS with MRFC and rigid coupling are conducted. Using the control variable method, the amplitude variation patterns of the different nodes of the MGTS under different currents and the vibration reduction effects of the MRFC and the traditional rigid coupling on the same node are compared. Figure 20 and 21 show the variations in the amplitudes of four nodes in the *x* and *y* directions when the MGTS is connected to different couplings under different currents, respectively.

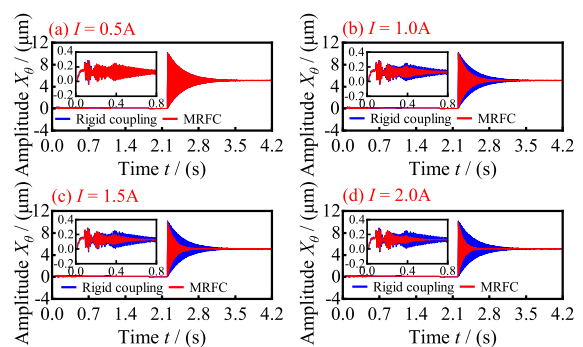
Figures 20 and 21(a)–(d) show that when the MRFC (the coil is connected with different currents) and the traditional rigid coupling are connected to the MGTS, the time domain variation patterns of the motor output shaft (node 4), bearing (node 8), driving gear (node 10), and driven gear (node 15) in the *x* and

*y* directions vary. Within 0–0.8 s, the motor starts and gradually completes the soft start process. In this stage, when the MGTS is connected to a traditional rigid coupling, the amplitude ranges of the four nodes in the *x* direction are  $-0.09$ – $0.04$   $\mu\text{m}$ ,  $-0.08$ – $0.05$   $\mu\text{m}$ ,  $-0.08$ – $0.035$   $\mu\text{m}$ , and  $-0.05$ – $0.09$   $\mu\text{m}$ , respectively. Those in the *y* direction are  $-0.04$ – $0.03$   $\mu\text{m}$ ,  $-0.03$ – $0.03$   $\mu\text{m}$ ,  $-0.02$ – $0.03$   $\mu\text{m}$ , and  $-0.02$ – $0.04$   $\mu\text{m}$ , respectively. As the coil current increases, the amplitude ranges of the four nodes decrease, with the greatest decrease occurring at a current of 0.5 A. At this current, the amplitude ranges of the four nodes in the *x* direction are  $-0.08$ – $0.03$   $\mu\text{m}$ ,  $-0.075$ – $0.04$   $\mu\text{m}$ ,  $-0.07$ – $0.02$   $\mu\text{m}$ , and  $-0.02$ – $0.06$   $\mu\text{m}$ , respectively. Those in the *y* direction are  $-0.02$ – $0.025$   $\mu\text{m}$ ,  $-0.02$ – $0.025$   $\mu\text{m}$ ,  $-0.015$ – $0.02$   $\mu\text{m}$ , and  $-0.01$ – $0.02$   $\mu\text{m}$ , respectively. Above 0.8 s, the MGTS is in a rated load operation stage. When the MGTS is connected to the traditional rigid coupling, the amplitude ranges of the four nodes in the *x* direction are  $-3.298$ – $0.3$   $\mu\text{m}$ ,  $-3.305$ – $0.213$   $\mu\text{m}$ ,  $-3.215$ – $0.195$   $\mu\text{m}$ , and  $-$

0.15–2.955  $\mu\text{m}$ , respectively. The amplitude ranges of the four nodes in the  $y$  direction are  $-1.127$ – $0.09$   $\mu\text{m}$ ,  $-1.336$ – $0.085$   $\mu\text{m}$ ,  $-1.04$ – $0.065$   $\mu\text{m}$ , and  $-0.086$ – $0.95$   $\mu\text{m}$ , respectively. When the MGTS is connected to the MRFC and the coil current is 0.5 A, the amplitude ranges of the four nodes in the  $x$  direction are  $-3.198$ – $0.285$   $\mu\text{m}$ ,  $-3.205$ – $0.185$   $\mu\text{m}$ ,  $-3.105$ – $0.125$   $\mu\text{m}$ , and  $-0.09$ – $2.585$   $\mu\text{m}$ , respectively. The amplitude ranges of the four nodes in the  $y$  direction are  $-1.155$ – $0.07$   $\mu\text{m}$ ,  $-1.03$ – $0.06$   $\mu\text{m}$ ,  $-0.95$ – $0.045$   $\mu\text{m}$ , and  $-0.07$ – $0.75$   $\mu\text{m}$ , respectively. When the coil current is 1.0 A, the amplitude ranges of the four nodes in the  $x$  direction are  $-2.877$ – $0.225$   $\mu\text{m}$ ,  $-2.65$ – $0.153$   $\mu\text{m}$ ,  $-2.75$ – $0.095$   $\mu\text{m}$ , and  $-0.07$ – $2.055$   $\mu\text{m}$ , respectively. The amplitude ranges of the four nodes in the  $y$  direction are  $-0.855$ – $0.05$   $\mu\text{m}$ ,  $-0.84$ – $0.049$   $\mu\text{m}$ ,  $-0.65$ – $0.0348$   $\mu\text{m}$ , and  $-0.05$ – $0.55$   $\mu\text{m}$ , respectively. When the coil current is 1.5 A, the amplitude range of the four nodes in the  $x$  direction are  $-2.26$ – $0.188$   $\mu\text{m}$ ,  $-2.16$ – $0.104$   $\mu\text{m}$ ,  $-2.37$ – $0.07$   $\mu\text{m}$ , and  $-0.04$ – $1.89$   $\mu\text{m}$ , respectively. The amplitude ranges of the four nodes in the  $y$  direction are  $-0.63$ – $0.035$   $\mu\text{m}$ ,  $-0.53$ – $0.033$   $\mu\text{m}$ ,  $-0.38$ – $0.021$   $\mu\text{m}$ , and  $-0.035$ – $0.45$   $\mu\text{m}$ , respectively. When the coil current is 2.0 A, the amplitude ranges of the four nodes in the  $x$  direction are  $-1.65$ – $0.116$   $\mu\text{m}$ ,  $-1.53$ – $0.084$   $\mu\text{m}$ ,  $-1.55$ – $0.04$   $\mu\text{m}$ , and  $-0.05$ – $1.57$   $\mu\text{m}$ , respectively. The amplitude ranges of the four nodes in the  $y$  direction are  $-0.42$ – $0.016$   $\mu\text{m}$ ,  $-0.28$ – $0.018$   $\mu\text{m}$ ,  $-0.22$ – $0.017$   $\mu\text{m}$ , and  $-0.02$ – $0.3$   $\mu\text{m}$ , respectively. The amplitude, amplitude range, and amplitude decay time of each node of the MGTS are reduced when the MRFC is connected to the MGTS at any current and at any time. This suggests that the MRFC has a suppression effect on the vibrations in the  $x$  and  $y$  directions of each node. The MRFC significantly reduces the amplitude fluctuations at each node and reduces the shock to the transmission system. Furthermore, as the coil current increases, the MRF apparent viscosity and shear modulus increase, the MRF stiffness and damping increase nonlinearly, the MRF shear stress increases, and the torque generated by the MRF increases. Therefore, the MRFC can be used in various workplaces and suppress vibrations. Figure 20 and 21 show that when the drive system is connected to the MRFC, node 15 has the best vibration suppression in the  $x$  and  $y$  directions, the fastest amplitude attenuation, and the most remarkable

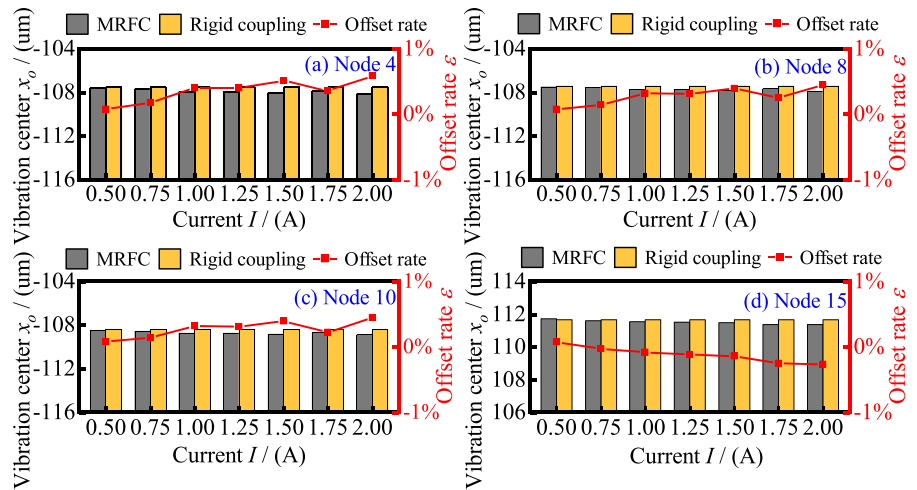
vibration reduction effect. Compared with the traditional rigid coupling, the MRFC can effectively suppress the vibrations of the helical gear system.

Fig. 22 (a), (b), (c) and (d) shows that when MRFC (The coil is connected with different currents) and traditional rigid coupling are connected to MGTS, respectively, the time domain variation pattern of the helical gear meshing node in the  $\theta$ -direction. In Fig. 22, when the MGTS is connected to a traditional rigid coupling, the amplitude range of the helical gear meshing node in the  $\theta$ -direction are:  $-0.036 \sim 11.25$   $\mu\text{m}$ , when the MGTS is connected to the MRFC and the coil current is 0.5A, the amplitude range of the helical gear meshing node in the  $\theta$ -direction is:  $-0.034 \sim 11.08$   $\mu\text{m}$ , the coil currents are, respectively: 1.0A, 1.5A, 2.0A, the amplitude range of the helical gear meshing node in the  $\theta$ -direction is, respectively:  $-0.022 \sim 10.32$   $\mu\text{m}$ ,  $-0.014 \sim 9.27$   $\mu\text{m}$ ,  $-0.007 \sim 8.04$   $\mu\text{m}$ . The MRFC compared with the traditional rigid coupling, the amplitude range decreases by 1.5%, 8.27%, 17.6%, 28.5%, respectively, at different coil currents, the MRFC can significantly reduce the amplitude range at the helical gear pairs meshing node. Furthermore, in different coil currents, the amplitude decay times of 2.8 s, 1.4 s, 0.9 s and 0.3 s, respectively, and as the coil current increases, the amplitude decay time at the helical gear mesh node decreases, the MGTS is in stable operation faster, and the stable operation time is longer, this indicates that the MRFC has superior vibration reduction and transmission performance. (a), (b), (c) and (d) in Fig. 23 and Fig. 24 show that when MRFC and traditional rigid coupling are connected to MGTS, respectively, the vibration center and the

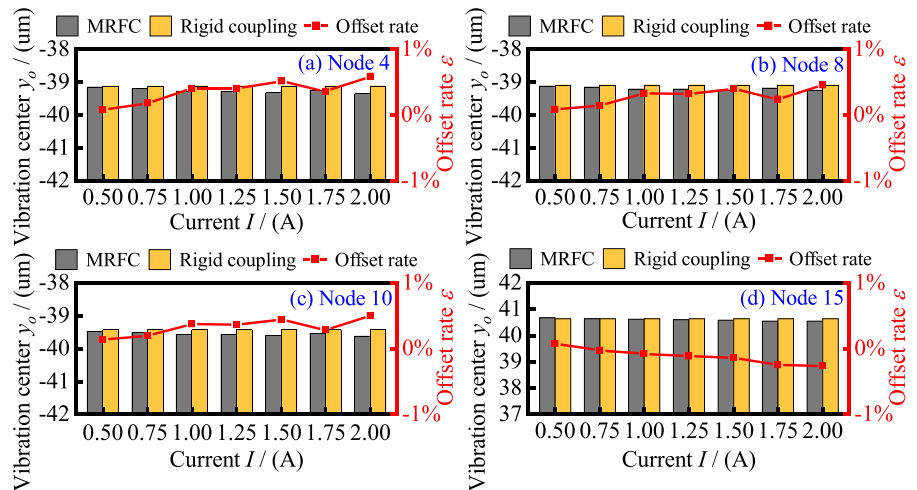


**Fig. 22** Displacement amplitude of helical gear meshing node in  $\theta$ -direction at different currents

**Fig. 23** Vibration center of four nodes in  $x$ -direction by different couplings



**Fig. 24** Vibration center of four nodes in  $y$ -direction by different couplings



RVCORs versus coil current pattern of the motor output shaft (node 4), the bearing (node 8), the driving gear (node 10) and the driven gear (node 15) in the  $x$ -direction and  $y$ -direction.

This study aims to more reasonably illustrate the vibration reduction effect of the MRFC on the MGTS and the extraordinary transmission performance of the MRFC and to avoid the influence of singularities generated by numerical simulations on the results discussed. Therefore, the data from the numerical simulations and presented in this paper are normalized. As described in Sect. 4.2, the numerical simulation data after 2.2 s (MGTS reaches the rated load time) are used for discussion and research. Figure 23 shows that when the MGTS is connected to the traditional rigid coupling, the vibration centers of the

four nodes in the  $x$  direction are  $-107.517 \mu\text{m}$ ,  $-107.417 \mu\text{m}$ ,  $-108.411 \mu\text{m}$ , and  $111.646 \mu\text{m}$ , respectively. When the MGTS is connected to the MRFC and the coil current is 2.0 A, the RVCORS of the four nodes in the  $x$  direction reach maximum

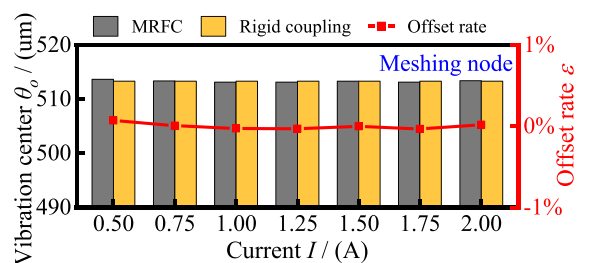


**Fig. 25** Vibration center of gear meshing node in  $\theta$  direction by different couplings

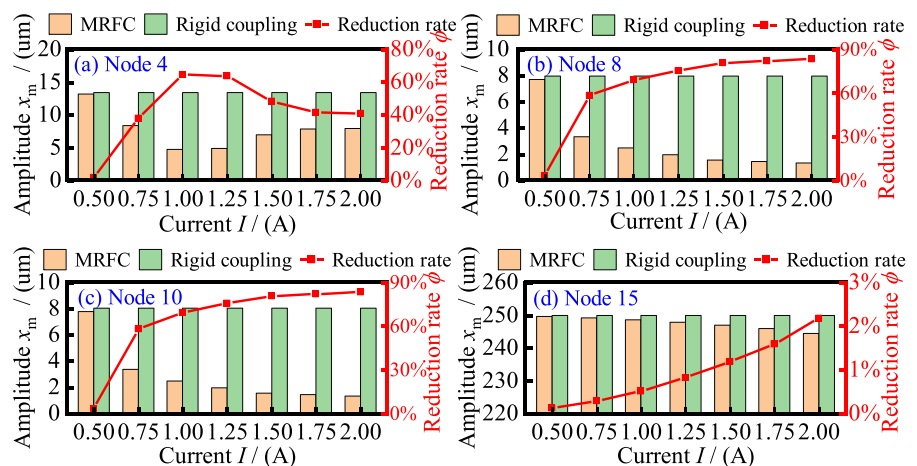
values of 0.586%, 0.447%, 0.446%, and  $-0.263\%$ , respectively. These correspond to the vibration centers reaching the extreme values of  $-108.147\ \mu\text{m}$ ,  $-107.897\ \mu\text{m}$ ,  $-108.895\ \mu\text{m}$ , and  $111.342\ \mu\text{m}$ , respectively. Figure 24 shows that when the MGTS is connected to the traditional rigid coupling, the vibration centers of the four nodes in the  $y$  direction are  $-39.132\ \mu\text{m}$ ,  $-39.094\ \mu\text{m}$ ,  $-39.438\ \mu\text{m}$ , and  $40.635\ \mu\text{m}$ , respectively. When the MGTS is connected to the MRFC and the coil current is 2.0 A, the RVCORs of the four nodes in the  $y$  direction reach maximum values of 0.586%, 0.451%, 0.497%, and  $-0.264\%$ , respectively. These correspond to the vibration centers reaching extreme values of  $-39.362\ \mu\text{m}$ ,  $-39.094\ \mu\text{m}$ ,  $-39.6343\ \mu\text{m}$ , and  $40.5286\ \mu\text{m}$ , respectively. Figure 23(d) and 24(d) show the vibration centers and the RVCORs versus coil current patterns of the driven gear node in the  $x$  and  $y$  directions when the MRFC and the traditional rigid coupling are connected to the MGTS. Noticeably, the torsional stiffness and torsional damping coefficient of the MRF increase significantly with increasing coil current. Therefore, the MRFC has the most significant effect on the RVCORs at this node. When the coil current increases from 0.5 to 2.0 A, for the offset of the driven gear node, the RVCORs drops rapidly from 0.0329% to  $-0.264\%$ . This suggests that when the MRFC reaches steady-state operation, the RVCORs of each node in the MGTS in the  $x$  and  $y$  directions have a nonlinear decreasing relationship with the coil current. Moreover, the MRFC has minimal influence on the vibration center of the driven gear node. As the coil current increases, the deflection

rates of the four nodes gradually decrease and approach constant (0). The MRFC hardly affects the vibration center of each mechanical part, and compared with the traditional rigid coupling, the MRFC does not change the vibration center and has superior vibration reduction and transmission performance.

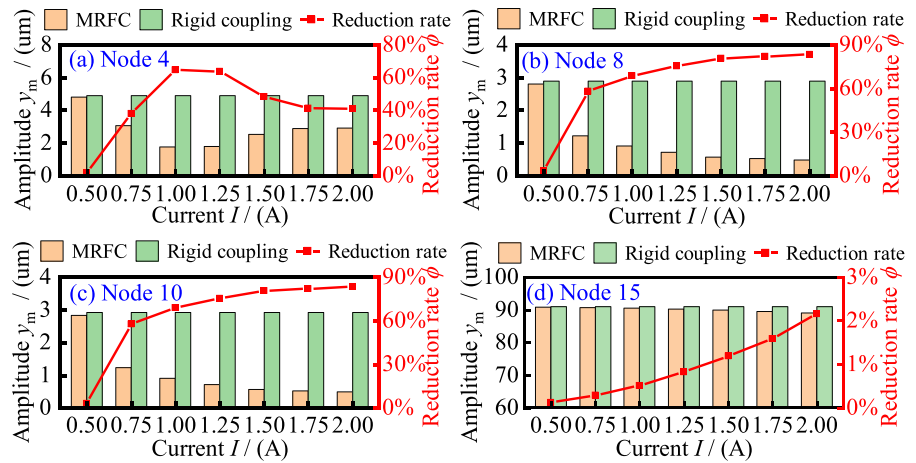
Figure 25 shows the vibration centers and the RVCORs versus coil current patterns of the helical gear meshing node in the  $\theta$  direction when the MRFC and the traditional rigid coupling are connected to the MGTS. When the MGTS is connected to the traditional rigid coupling, the vibration center of the helical gear meshing node in the  $\theta$  direction is  $513.329\ \mu\text{m}$ . When the MGTS is connected to the MRFC and the coil current is 0.5 A, the RVCORs of the helical gear meshing node in the  $\theta$  direction reach a maximum value of 0.0722%. In contrast, when the coil current is 2.0 A, it reaches a minimum value of 0.0194%. These correspond to the vibration center reaching the extreme values of  $513.70\ \mu\text{m}$  and  $513.429\ \mu\text{m}$ , respectively. The variation trends of the RVCORs of the helical gear mesh node in the  $\theta$  direction and coil current are consistent with those of the driven gear in the  $x$  and  $y$  directions; however, the MRFC has the least impact on the vibration center of the helical gear mesh node. This suggests that when the MRFC reaches a stable operation state, it does not affect the vibration center of helical gear meshing part and cannot change its RVCORs.

Figure 26 shows the maximum amplitudes and maximum vibration amplitude reduction rates (MVARRs) of the four nodes in the  $x$  direction versus the coil current when the MRFC and the traditional

**Fig. 26** Maximum vibration amplitudes of four nodes in  $x$  direction by different couplings



**Fig. 27** Maximum vibration amplitude of four nodes in y-direction by different couplings



rigid coupling are connected to the MGTS. Noticeably, the maximum vibration amplitude of each node decreases and the MVARRs increases approximately linearly with the increase in the current when the MRFC is connected to the system. Node 4 is the motor output node, and owing to the unique rheological characteristics of the MRF, at a low current, the MRFC can achieve no-load starting of the motor, reducing the shock load. Therefore, when the current is 0.5 A, the maximum vibration amplitude of node 4 is smaller than when the traditional rigid coupling is connected during startup. Moreover, at a low, the maximum vibration amplitudes of the remaining nodes are slightly larger than those when the rigid coupling is connected. These amplitudes at 0.5 A are 13.188  $\mu\text{m}$ , 7.694  $\mu\text{m}$ , 7.762  $\mu\text{m}$ , and 249.597  $\mu\text{m}$ , respectively. As the current increases and the MRFC is connected, the maximum vibration amplitude of each node gradually decreases, reaching minimum values of 4.766  $\mu\text{m}$ , 1.316  $\mu\text{m}$ , 1.325  $\mu\text{m}$ , and 244.466  $\mu\text{m}$ , respectively, when the current is 2.0 A. Concurrently, and the MVARRs of the nodes reach maximum values of 40.98%, 83.4%, 83.49%, and 2.17%, respectively. These results suggest that the MRFC significantly reduces the maximum vibration amplitude of each node compared with the traditional rigid coupling, suppresses the vibrations of the transmission system, and decreases the impact of the shock load during motor startup.

Figure 27 shows the maximum amplitude and MVARRs of the four nodes in the y direction versus the coil current when the MRFC and the traditional rigid coupling are connected to the MGTS. The

variation patterns of the MVARRs of the four nodes in the y direction versus the current are the same as those in the x direction. At a current of 0.5 A, because the MRFC can soft start the motor, the maximum vibration amplitude of node 4 is significantly smaller than that of the traditional rigid coupling at startup. When the current is below 0.75 A, the maximum vibration amplitudes of the remaining nodes with the MRFC are slightly greater than those with the traditional rigid coupling. At 0.5 A, the maximum vibration amplitudes of the four nodes reach maximum values of 4.8  $\mu\text{m}$ , 2.8  $\mu\text{m}$ , 2.825  $\mu\text{m}$ , and 90.846  $\mu\text{m}$ , respectively. As the current increases and the MRFC is connected, the maximum vibration amplitude of each node gradually decreases. When the current is 2.0 A, the maximum vibration amplitudes of the four nodes reach values of 2.88  $\mu\text{m}$ , 0.478  $\mu\text{m}$ , 0.482  $\mu\text{m}$ , and 88.988  $\mu\text{m}$ , respectively. Concurrently, the MVARRs of the nodes reach maximum values of 64.4%, 83.4%, 83.46%, and 2.16%, respectively. This suggests that the MRFC can significantly reduce the maximum vibration amplitude of each node compared with the traditional rigid coupling and also suppress the vibrations of the transmission system. The maximum vibration amplitude suppression effect of the MRFC on nodes 4, 8, and 10 in the x and y directions is significant. The torsional stiffness and damping of the MRFC increase as the current increases, and concurrently, the vibration reduction in the MGTS becomes more significant (Fig. 28).

As an important component of the MGTS, the helical gear pair carries the role of the transmission system, Therefore, for a stabler output load, the helical

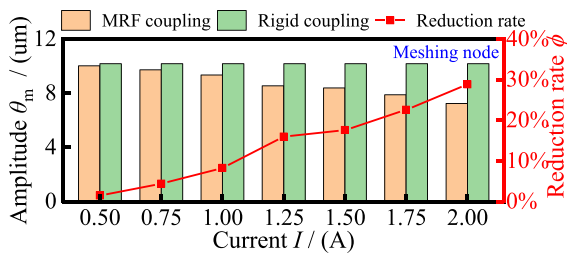


**Fig. 28** Maximum vibration amplitudes of gear meshing node in  $\theta$  direction by different couplings

gear pair vibration should be as small as possible. Figure 26 shows the maximum amplitudes and MVARRs of the helical gear pair meshing node in the  $\theta$  direction versus the coil current when the MRFC and the traditional rigid coupling are connected to the MGTS. As the current increases, the torsional vibration of the helical gear node gradually decreases, and the MVARRs in the  $\theta$  direction increase gradually. When the coil current is 2.0 A, the MVARRs reaches a maximum value of 29.1%. Comparing Figs. 26(a)–(c) and 27(a)–(c), the MVARRs of each node in the  $x$  and  $y$  directions are significantly greater than those in the  $\theta$  direction.

## 5 Conclusion

In this study, a mechanical–electromagnetic coupled dynamics model of an MGTS is established; the dynamics model includes a drive motor, a gear transmission system, an MRFC, and a load. Based on the model, the influence of the MRFC coil current variation on the dynamic response characteristics and vibration reduction in the system is investigated during the startup and stable operation stages of the drive motor. The research results showed the following:

- (1) The coil current exhibits a temporary overshoot phenomenon for a duration 120 ms, following which it tends to stabilize. Concurrently, the coil current overshoot rate gradually increases with increasing coil current from 0.5 A to 2.0 A, and these rates at different currents are 2.2%, 4.75%, 6.86%, and 8.84%, respectively. Similarly, the magnetic flux density and magnetic field intensity of the MRFC working gap also increase with increasing coil current. Moreover, their

distributions are axisymmetric, resulting in the torque transmitted by the MRFC to increase from 70 N·m to 115 N·m. However, the dynamic response time of the torque reduces from 0.125 s to 0.002 s.

- (2) As the coil current increases, the RVCORs of each component gradually decrease, and it is slightly lower in the  $y$  direction than that in the  $x$  direction. When the coil current is 2.0 A, the RVCORs of nodes 4, 8, 10, and 15 in the  $x$  and  $y$  directions are maximum; their values are 0.586%, 0.447%, 0.446%, and  $-0.263\%$ , respectively, and 0.586%, 0.451%, 0.497%, and  $-0.264\%$ , respectively. Concurrently, the RVCORs of the helical gear meshing node in the  $\theta$  direction also reach a maximum with a value of 0.0194%.
- (3) In the drive motor startup stage, at different coil currents, the vibration amplitude fluctuation ranges produced by the MRFC are smaller than those by the traditional rigid coupling. Moreover, compared with the traditional rigid coupling, with the MRFC, the vibration amplitude fluctuation ranges of nodes 4, 8, 10, and 15 in the  $x$  and  $y$  directions present significant reduction. In the  $x$  direction, the ranges reduce from  $-0.09$ – $0.04 \mu\text{m}$  to  $-0.08$ – $0.03 \mu\text{m}$ , from  $-0.08$ – $0.05 \mu\text{m}$  to  $-0.075$ – $0.04 \mu\text{m}$ , from  $-0.08$ – $0.035 \mu\text{m}$  to  $-0.07$ – $0.02 \mu\text{m}$ , and from  $-0.05$ – $0.09 \mu\text{m}$  to  $-0.02$ – $0.06 \mu\text{m}$ , respectively. In the  $y$  direction, the ranges decrease from  $-0.04$ – $0.03 \mu\text{m}$  to  $-0.02$ – $0.025 \mu\text{m}$ , from  $-0.03$ – $0.03 \mu\text{m}$  to  $0.02$ – $0.025 \mu\text{m}$ , from  $-0.02$ – $0.03 \mu\text{m}$  to  $-0.015$ – $0.02 \mu\text{m}$ , and from  $-0.02$ – $0.04 \mu\text{m}$  to  $-0.01$ – $0.02 \mu\text{m}$ , respectively.
- (4) In drive motor stable operation stage, the vibration amplitude fluctuation ranges produced by the MRFC are smaller than those by the traditional rigid coupling, and the maximum vibration amplitude of each component decreases with increasing coil current. Conversely, the MVARRs increases with increasing coil current. When the coil current is 2.0 A, the MVARRs of each node reach maximum. For example, the MVARRs of nodes 4, 8, 10, and 15 in the  $x$  and  $y$  directions are 40.98%, 83.4%, 83.49%, and 2.17%, respectively, and 64.4%, 83.4%, 83.46%, and 2.16%, respectively. The



MVARRs of the helical gear meshing node in the  $\theta$  direction are 29.1%. Moreover, when the coil current changes from 0.5 A to 2.0 A, the amplitude decay time of the helical gear meshing node in the  $\theta$  direction becomes increasingly shorter, from 2.8 s to 0.3 s.

The research results provide a theoretical basis for using an MRFC in an MGTS to suppress vibrations and provide stable and reliable output torque. Moreover, it offers a design reference for the application of MRF damping devices for vibration and noise reduction in transmission systems. Concurrently, the dynamic performance of an MRF is influenced by temperature; therefore, in future studies, we will pay more attention to this effect on the dynamic characteristics and vibration reduction in an MRFC.

**Acknowledgements** The authors would like to gratefully acknowledge the National Natural Science Foundation of China (51905060); Open Fund of the State Key Laboratory of Mechanical Transmission (SKLMT-MSKFKT-202119); China's National Natural Science Foundation (52275052/51905064/52105245/51875068); China Postdoctoral Science Foundation (2021M700619/2022MD713697); Natural Science Foundation Project of Chongqing Science and Technology Commission (cstc2020jcyj-msxmX0346/cstc2021jcyj-msxmX0361); Science and Technology Research Program of Chongqing Municipal Education Commission (KJQN201901107).

**Data availability** Data sharing is not applicable to this article as no datasets were generated or analyzed during the current study.

## References

- De Vicente, J., Klingenberg, D.J., Hidalgo-Alvarez, R.: Magnetorheological fluids: a review. *Soft Matter* **7**(8), 3701–3710 (2011)
- Park, B.J., Fang, F.F., Choi, H.J.: Magnetorheology: materials and application. *Soft Matter* **6**(21), 5246–5253 (2010)
- Rodríguez-López, J., Elvira, L., Resa, P., et al.: Sound attenuation in magnetorheological fluids. *J. Phys. D Appl. Phys.* **46**(6), 065001 (2013)
- Ahamed, R., Choi, S.-B., Ferdaus, M.M.: A state of art on magneto-rheological materials and their potential applications. *J. Intell. Mater. Syst. Struct.* **29**(10), 2051–2095 (2018)
- Lee, C.H., Lee, D.W., Choi, J.Y., et al.: Tribological characteristics modification of magnetorheological fluid. *J. Tribol* **133**(3), 031801 (2011)
- Olivier, M., Pacifique, T., Jongseok, O., et al.: Design and analysis of a hybrid annular radial magnetorheological damper for semi-active in-wheel motor suspension. *Sensors* **22**(10), 3689 (2022)
- Kobayashi, M., Shi, F., Maemori, K.-I.: Modeling and parameter identification of a shock absorber using magnetorheological fluid. *J. Syst. Des. Dyn.* **3**, 804–813 (2009)
- Ashok, K.K., Hemantha, K., Arun, M.: Effect of temperature on sedimentation stability and flow characteristics of magnetorheological fluids with damper as the performance analyser. *J. Magn. Magn. Mater.* **555**, 169342 (2022)
- Zhongqiang, F., Dong, Y., Zhaobo, C., et al.: An improved constant deceleration control method with extended shock velocity range for magnetorheological energy absorber. *J. Intell. Mater. Syst. Struct.* **33**(12), 1513–1526 (2021)
- Yi, Y., Qin, D., Liu, C.: Investigation of electromechanical coupling vibration characteristics of an electric drive multistage gear system. *Mech. Mach. Theory* **121**, 446–459 (2018)
- Liu, C., Yin, X., Liao, Y., et al.: Hybrid dynamic modeling and analysis of the electric vehicle planetary gear system. *Mech. Mach. Theory* **150**, 103860 (2020)
- Chen, X., Hu, J., Chen, K., et al.: Modeling of electromagnetic torque considering saturation and magnetic field harmonics in permanent magnet synchronous motor for HEV. *Simul. Model. Pract. Theory* **66**, 212–225 (2016)
- Jiang, S., Li, W., Wang, Y., et al.: Study on electromechanical coupling torsional resonance characteristics of gear system driven by PMSM: a case on shearer semi-direct drive cutting transmission system. *Nonlinear Dyn.* **104**(2), 1205–1225 (2021)
- Jiang, Y., Zhu, H., Li, Z., et al.: The nonlinear dynamics response of cracked gear system in a coal cutter taking environmental multi-frequency excitation forces into consideration. *Nonlinear Dyn.* **84**(1), 203–222 (2015)
- Zhu, W., Wu, S., Wang, X., et al.: Harmonic balance method implementation of nonlinear dynamic characteristics for compound planetary gear sets. *Nonlinear Dyn.* **81**(3), 1511–1522 (2015)
- Li, Z., Peng, Z.: Nonlinear dynamic response of a multi-degree of freedom gear system dynamic model coupled with tooth surface characters: a case study on coal cutters. *Nonlinear Dyn.* **84**(1), 271–286 (2015)
- Wang, J., He, G., Zhang, J., et al.: Nonlinear dynamics analysis of the spur gear system for railway locomotive. *Mech. Syst. Signal Process.* **85**, 41–55 (2017)
- Li, S., Wu, Q., Zhang, Z.: Bifurcation and chaos analysis of multistage planetary gear train. *Nonlinear Dyn.* **75**(1), 217–233 (2014)
- Zhibo, G., Junyang, L., Ke, X., et al.: Analysis on the vibration reduction for a new rigid–flexible gear transmission system. *J. Vib. Control* **28**(17–18), 2212–2225 (2022)
- Lee, Y.K., Jun, J.H., Choi, C.S.: Damping capacity in Fe-Mn binary alloys. *Trans. Iron Steel Inst. Japan* **37**(10), 1023–1030 (1997)
- Ma, H., Yang, J., Song, R., et al.: Effects of tip relief on vibration responses of a geared rotor system. *Proc. Inst. Mech. Eng. Part C J. Mech. Eng. Sci.* **228**(7), 1132–1154 (2014)
- Bonori, G., Barbieri, M., Pellicano, F.: Optimum profile modifications of spur gears by means of genetic algorithms. *J. Sound Vib.* **313**(3), 603–616 (2008)

23. Xu, G., Dai, N., Tian, S.: Principal stress lines based design method of lightweight and low vibration amplitude gear web. *Math. Biosci. Eng.* **18**(6), 7060–7075 (2021)
24. Xiao, W., Li, J., Wang, S., et al.: Study on vibration suppression based on particle damping in centrifugal field of gear transmission. *J. Sound Vib.* **366**, 62–80 (2016)
25. Ramadani, R., Belsak, A., Kegl, M., et al.: Topology optimization based design of lightweight and low vibration gear bodies. *Int. J. Simul. Modell.* **17**, 92–104 (2018)
26. Wang, Y.-L., Cao, D. Q., Wang, Q.-Y., et al.: Torsional vibration suppression of a gear system installed with a damping ring (2017)
27. Bossis, G., Lacin, S., Meunier, A., et al.: Magnetorheological fluids. *J. Magn. Magn. Mater.* **252**, 224–228 (2002)
28. Huang, J., Zhang, J.Q., Yang, Y., et al.: Analysis and design of a cylindrical magneto-rheological fluid brake. *J. Mater. Process. Technol.* **129**(1–3), 559–562 (2002)
29. Hoang, N., Zhang, N., Du, H.: An adaptive tunable vibration absorber using a new magnetorheological elastomer for vehicular powertrain transient vibration reduction. *Smart Mater. Struct.* **20**(1), 015019 (2010)
30. Hoang, N., Zhang, N., Du, H.: A dynamic absorber with a soft magnetorheological elastomer for powertrain vibration suppression. *Smart Mater. Struct.* **18**(7), 074009 (2009)
31. Shu, R., Wei, J., Tan, R., et al.: Investigation of dynamic and synchronization properties of a multi-motor driving system: theoretical analysis and experiment. *Mech. Syst. Signal Process.* **153**, 107496 (2021)
32. Zhang, A., Wei, J., Shi, L., et al.: Modeling and dynamic response of parallel shaft gear transmission in non-inertial system. *Nonlinear Dyn.* **98**(2), 997–1017 (2019)
33. Chen, S., Tang, J., Li, Y., et al.: Rotordynamics analysis of a double-helical gear transmission system. *Meccanica* **51**(1), 251–268 (2016)
34. Wei, J., Zhang, A., Qin, D., et al.: A coupling dynamics analysis method for a multistage planetary gear system. *Mech. Mach. Theory* **110**, 27–49 (2017)
35. Hu, Z., Tang, J., Zhong, J., et al.: Frequency spectrum and vibration analysis of high speed gear-rotor system with tooth root crack considering transmission error excitation. *Eng. Fail. Anal.* **60**, 405–441 (2016)
36. Shu, R.: Electromechanical coupling dynamic characteristic and optimization of new shearer cutting short-range transmission system. Chongqing University (2018)
37. Xiong, Y., Huang, J.: A novel magnetorheological braking system with variable magnetic particle volume fraction-controlled by utilizing shape memory alloy. *J. Intell. Mater. Syst. Struct.* **34**, 3–14 (2022)

**Publisher's Note** Springer Nature remains neutral with regard to jurisdictional claims in published maps and institutional affiliations.

Springer Nature or its licensor (e.g. a society or other partner) holds exclusive rights to this article under a publishing agreement with the author(s) or other rightsholder(s); author self-archiving of the accepted manuscript version of this article is solely governed by the terms of such publishing agreement and applicable law.